

Article

Impact of the Atmospheric Photochemical Evolution of the Organic Component of Biomass Burning Aerosol on Its Radiative Forcing Efficiency: A Box Model Analysis

Tatiana B. Zhuravleva ^{1,*} , Ilmir M. Nasrtdinov ¹ , Igor B. Konovalov ² , Nikolai A. Golovushkin ² and Matthias Beekmann ³

¹ V.E. Zuev Institute of Atmospheric Optics SB RAS, Academician Zuev Square, 1, 634055 Tomsk, Russia; wizard@iao.ru

² Institute of Applied Physics of the Russian Academy of Sciences, 46 Ul'yanov Str., 603950 Nizhny Novgorod, Russia; konov@ipfran.ru (I.B.K.); golovushkin@ipfran.ru (N.A.G.)

³ Laboratoire Inter-Universitaire des Systèmes Atmosphériques (LISA), CNRS, 75016 Paris, France; beekmann@lisa.ipsl.fr

* Correspondence: ztb@iao.ru

Abstract: We present the first box model simulation results aimed at identification of possible effects of the atmospheric photochemical evolution of the organic component of biomass burning (BB) aerosol on the aerosol radiative forcing (ARF) and its efficiency (ARFE). The simulations of the dynamics of the optical characteristics of the organic aerosol (OA) were performed using a simple parameterization developed within the volatility basis set framework and adapted to simulate the multiday BB aerosol evolution in idealized isolated smoke plumes from Siberian fires (without dilution). Our results indicate that the aerosol optical depth can be used as a good proxy for studying the effect of the OA evolution on the ARF, but variations in the scattering and absorbing properties of BB aerosol can also affect its radiative effects, as evidenced by variations in the ARFE. Changes in the single scattering albedo (SSA) and asymmetry factor, which occur as a result of the BB OA photochemical evolution, may either reduce or enhance the ARFE as a result of their competing effects, depending on the initial concentration OA, the ratio of black carbon to OA mass concentrations and the aerosol photochemical age in a complex way. Our simulation results also reveal that (1) the ARFE at the top of the atmosphere is not significantly affected by the OA oxidation processes compared to the ARFE at the bottom of the atmosphere, and (2) the dependence of ARFE in the atmospheric column and on the BB aerosol photochemical ages almost mirrors the corresponding dependence of SSA.

Keywords: biomass burning; organic aerosol; microphysical model; volatility basis set; Mie theory calculations; radiative transfer model; aerosol radiative forcing efficiency



Citation: Zhuravleva, T.B.; Nasrtdinov, I.M.; Konovalov, I.B.; Golovushkin, N.A.; Beekmann, M. Impact of the Atmospheric Photochemical Evolution of the Organic Component of Biomass Burning Aerosol on Its Radiative Forcing Efficiency: A Box Model Analysis. *Atmosphere* **2021**, *12*, 1555. <https://doi.org/10.3390/atmos12121555>

Academic Editor: Gloria Titos

Received: 18 October 2021

Accepted: 22 November 2021

Published: 24 November 2021

Publisher's Note: MDPI stays neutral with regard to jurisdictional claims in published maps and institutional affiliations.



Copyright: © 2021 by the authors. Licensee MDPI, Basel, Switzerland. This article is an open access article distributed under the terms and conditions of the Creative Commons Attribution (CC BY) license (<https://creativecommons.org/licenses/by/4.0/>).

1. Introduction

Biomass burning (BB), in the form of open forest and peat fires, is one of the largest sources of many trace gases and aerosols to the global atmosphere. For some important components atmospheric aerosol, like black carbon (BC) and organic compounds biomass burning accounts, according to estimates of Bond et al. [1], for 40% of BC and 85% of organic carbon emissions worldwide. Biomass burning aerosol contributes considerably to the radiation budget of the atmosphere and surface and, as such, should be accounted for adequately in climate simulations and assessments of the radiative forcing, determined by anthropogenic emissions [1–7].

As a result of hundreds of observational studies involving in situ measurements and remote sensing with the ground-, aircraft- and satellite-based instruments, a large amount of data on characteristics of carbonaceous particles has been collected and reported since the 1990s. However, even with the availability of such voluminous data, the quantification

of the key parameters for estimating radiative effects of BB aerosol is not straightforward, primarily because the smoke properties are highly variable, depending on a variety of factors such as the type of biomass, the combustion temperature, meteorological conditions, atmospheric age of the smoke, etc. (see, e.g., results of research of BB aerosol in major BB regions of the world [8–15], corresponding reviews [16–21] and bibliography therein).

Commonly, the radiative effects of atmospheric aerosol in the “atmosphere-underlying surface” system on global and regional scales are studied using chemistry-transport models of various complexities and much more comprehensive Earth system models. However, a reliable representation of the radiative properties of BB aerosol in these models is conditioned by the adequate description of its optical properties, which is very challenging to ensure due to strong variability of the chemical composition and microphysical structure of BB aerosol particles, in part due to the atmospheric evolution of the organic component of aerosol. Following a common convention, we refer below to this component as organic aerosol (OA). The atmospheric evolution (or, in other words, atmospheric aging) of OA has been found in laboratory experiments and in the real atmosphere to be associated with a variety of observable manifestations, such as a substantial increase or decrease in the mass fraction of OA in BB smoke [22–25], an increase in the oxidation state and hygroscopicity of BB aerosol particles [26–28], changes in the absorption characteristics of aerosol due to destruction or formation of brown carbon [29,30], an increase in scattering and extinction efficiencies and single scattering albedo [31–34].

However, although the transformations of BB OA due to its atmospheric aging are commonly recognized to be among important factors that determine the observed variability in the BB aerosol optical and radiative properties, they have been either disregarded or represented in extremely simplified and rather arbitrary ways in most of the model studies of the radiative and climate effects of BB aerosol, contributing to the considerable uncertainty in model results [2–6,35–37]. Constraining this uncertainty requires a good knowledge of the key factors and mechanisms, through which the processes driving the atmospheric evolution of BB OA can affect its radiative properties. Such processes are known to encompass thousands of different organic species and include, in particular, secondary OA (SOA) formation through functionalization oxidation reactions, consecutive multistage oxidation of SOA, which eventually leads to the destruction of SOA through fragmentation reactions, as well as volatilization of primary and secondary OA as a result of dilution of primary emissions in the atmosphere [38–40].

One of the useful approaches allowing isolating and better understanding—at least at a qualitative level—of various effects of these processes involves the analysis based on the use of box models [41–47]. In particular, this approach allowed identifying qualitative features of the response of the behavior of BB OA mass concentration within an isolated smoke plume to changes in several key parameters, such as the fire size, initial concentration of BB aerosol, and the background aerosol concentration [44–46]. It has also been suggested that variations in the fire size and background aerosol concentration can significantly influence the radiative forcing of BB aerosol (ARF), assuming that changes in the ARF are directly related to the changes in aerosol extinction cross-section [45]. However, to the best of our knowledge, possible qualitative effects of the atmospheric transformations of BB aerosol on the radiative forcing have not yet been systematically analyzed beyond the simplifying assumption that the changes in ARF are directly proportional to changes in the aerosol extinction cross-section.

This study is aimed at achieving a better understanding of the possible effects of the atmospheric evolution of the organic component of BB aerosol on its radiative properties. More specifically, a goal of our study is to investigate whether the BB aerosol aging can be associated with significant changes in its radiative forcing efficiency (ARFE), which is defined as ARF of BB aerosol per unit of its extinction optical depth and allows one to compare the radiative properties of various aerosols irrespectively of a magnitude of the aerosol optical depth (e.g., [48]). The study is based on the use of a microphysical box model [46], which was designed to represent the atmospheric evolution of OA in

an idealized isolated BB plume by taking into account oxidation processes as well as condensational growth and evaporation of particles [1]. The oxidation and volatilization of OA matter are represented within the volatility basis set (VBS) framework [38]. We use a simple VBS scheme that was optimized previously using satellite observations and chemistry-transport model simulations of the long-range transport of BB plumes from Siberia [34]. Hence, our analysis primarily addresses the radiative properties of specifically Siberian BB aerosol. Note that the use of a simple VBS scheme is justifiable by the fact that there is presently no validated and generally accepted method to simulate the atmospheric evolution of BB aerosol, whereas different available methods yield diverse results [36,49]. Taking into account that our modeling framework is highly simplified, we do not attempt to obtain accurate quantitative estimates of the radiative properties of BB aerosol, but rather aim at identifying only qualitative features of the evolution of the radiative forcing efficiency of BB aerosol in an idealized smoke plume. More specifically, we focus on the changes in ARFE due to the oxidation of organic compounds within the BB plume. We believe that the knowledge of these features will help to predict and interpret a possible diversity and uncertainty in quantitative assessments of ARF based on much more complex simulations with chemistry-transport and climate models.

2. Methods

2.1. Simulations of the BB Aerosol Evolution

The atmospheric evolution of OA was simulated using the Microphysical Dynamic Model of Organic Aerosol (MDMOA) [46]. This is a box model that solves a system of dynamic equations for concentrations of carbonaceous components of multi-disperse aerosol in a diluting BB smoke plume. The model system includes, in particular, the equations that describe the changes in mass concentration of semivolatile organic compounds (SVOCs) in a given particle size section due to the mass transfer between the condensed phase and gas phase of a given compound using the Fuchs–Sutugin approximation for the condensational growth of particles. These equations take into account that the condensation and evaporation processes determining the mass transfer can result not only in changes in OA concentration but also in modifications of the size distribution of particles. The dynamics of the total (both condensed and gas phase) concentration of a given compound is governed by kinetic equations that take into account the oxidation processes described below. The formulations of the dynamic equations can be found elsewhere [46].

As noted above, the analysis performed in this study is focused on the effects of oxidation processes on the BB aerosol radiative properties. To isolate these effects, we disregarded any other processes that can affect the evolution of the radiative properties of BB aerosol. In particular, following our previous box model study of the BB aerosol evolution [46], we disregarded coagulation and deposition of the particles. Furthermore, we assumed (also following [46]) that the BB aerosol particles consist of only carbonaceous material. That is, the contributions of inorganic salts and water to the particle composition were disregarded. Note that optically dense smoke plumes are typically observed in Siberia in a relatively dry atmosphere with RH less than 70% [49], whereas the water uptake by BB aerosol particles under such conditions is indeed likely to be small [50], and it is also known that inorganic salts typically constitute a minor fraction of BB aerosol [51]. Finally, we also disregarded the dilution. It has previously been suggested [21,45,46] that the dilution can considerably complicate the behavior of both mass concentration and optical properties of BB OA since the acceleration of particle evaporation due to dilution depends on the OA composition and oxidation state in a complex manner. Presuming that the dilution rate is inversely dependent on the plume size [44,46], disregarding the effect of the dilution seems to be a reasonable zero-order approximation in the case of large-scale (and thus slowly diluting) plumes (similar, e.g., to those analyzed that propagated from Siberia into the European part of Russia the Siberian plume in summer 2016 [34]), although the dilution can hardly be disregarded completely in any real situation. Overall, our box model simulations address a highly simplified and idealized situation and are not expected

to provide a quantitatively accurate representation of the complex atmospheric evolution of OA in any specific real BB plumes. However, we consider the simplification of the complex aerosol system as a key prerequisite for achieving a better understanding of the complex effects addressed in this study. Possible implications of the results of our analysis for understanding the evolution of the radiative properties of real BB aerosol are discussed in Section 4.

The chemical evolution of thousands of real organic compounds, resulting in changes in the volatility of the organic matter in BB aerosol particles, is represented in our model within the volatility base set framework [38] by splitting all SVOCs into several classes, s , with different volatilities (saturation concentrations), C_s^* . Within this framework, the equilibrium gas-phase concentration for a given species (C_s^{eq}) is inversely dependent on the total mass concentration of the organic compounds in particles, C_{OA} , and determined as follows:

$$C_s^{eq} = C_s^* \frac{f_s C^{tot}}{C_{OA}} \left(1 + \frac{C^{tot}}{C_{OA}} \right)^{-1}, \quad (1)$$

where f_s is the mass fraction of a given species, C^{tot} is the total (gas-phase and condensed-phase) mass concentration of SVOCs. The initial value of C_{OA} (corresponding to instantaneous thermodynamic equilibrium) was considered as one of the control parameters of our numerical experiments and is denoted below as C_0 .

We used a simplified adjustable VBS scheme, which was introduced in our recent study [34] and is denoted below as K21. Although several other VBS schemes of various complexity have been proposed in the literature to model the atmospheric evolution of BB OA (see, e.g., [24,39,43,47,52–54]), neither of them have been validated against observations of changes in the physical or optical properties of OA during its multiday evolution in Siberian BB plumes (even though most of them were found to enable a reasonable agreement of OA simulations with selected sets of ground-based and satellite observations of BB aerosol in various regions of the world). The key advantage of the K21 scheme is that it was shown to adequately reproduce the multiday dynamics of the aerosol optical depth (AOD) in BB plumes originating from forest fires in Siberia [34]. Furthermore, the simulations with MDMOA using the K21 scheme were found [34] to be in a reasonable agreement with data from chamber experiments [43]. Note that the K21 scheme was derived from a more complex “1.5-dimensional” VBS scheme which was originally optimized against the same chamber data [43]. The simplified character of the K21 scheme reflects the high variability of the composition of real BB plumes in Siberia [9] and the lack of knowledge that would allow reproducing this variability in models. Accordingly, our box model simulations are supposed to provide a qualitative description of the photochemical aging of BB aerosol within a typical large-scale plume that encompasses emissions from multiple Siberian fires corresponding to different vegetation land cover types.

In the K21 scheme, primary and secondary SVOCs are split into two and three volatility classes, respectively. The scheme also includes one species representing a source of SVOCs from oxidation of volatile organic compounds (VOCs). Following multiple previous studies involving the VBS framework to model the atmospheric evolution of BB OA aerosol (e.g., [39, 43,47,52–54]), we describe the chemical evolution of the model species by considering their gas-phase oxidation reactions with the hydroxyl radical (OH). The OH reactions are assumed to effectively represent oxidation of organic compounds by other oxidants, such as ozone (O_3) and nitrate radical (NO_3). Note that although both the O_3 and NO_3 oxidation can provide important sources of SOA, especially when O_3 concentration is very high [55] or in a dark atmosphere [56], to the best of our knowledge, there have been no observational or laboratory data that could provide strong constraints on the effects of these oxidants on the evolution of BB aerosol optical properties in the real atmosphere. Nonetheless, since the K21 scheme was constrained by satellite observations of Siberian BB aerosol during its long-range transport [34], a possible impact of the dark aging of BB OA (specifically, during

relatively short nighttime periods in middle latitudes in July) on the multiday evolution of the optical properties is implicitly taken into account in our simulations.

The oxidation of primary organic aerosol species is described by functionalization reactions yielding low-volatility SOA species and enhancing the OA mass concentration. The oxidation of VOCs also leads to the formation of SOA species. These species are further oxidized through both functionalization and fragmentation reactions, resulting in both the formation of less volatile SOA species and a partial loss of the SOA mass concentration. An in-detail description of our VBS scheme can be found elsewhere [34].

Apart from organic compounds, the particle composition is assumed to include BC, which is treated as a chemically inert and nonvolatile species. The mass ratio of BC and OA (the BC/OA ratio) in fresh BB aerosol is considered as one more control parameter in our numerical experiments.

Our runs of MDMOA covered 120 h. The initial conditions for SVOCs in particles and the gas phase were specified following the gas-particle equilibrium determined by the partitioning theory. The particles were distributed among nine size sections from 10 nm to 10 μm following the lognormal distribution with a mass median diameter of 0.3 μm and a geometric standard deviation of 1.6 [16]. Following previous box model studies [44–46], we assume that the OH concentration keeps constant during the daytime plume evolution and drops to zero during the nighttime. For definiteness, its value was set to $5 \times 10^6 \text{ cm}^{-3}$ in our simulations, partly based on aircraft measurements within BB plumes in North America [32]. Hence, any changes in the BB aerosol properties are assumed to occur only during the daytime, and so the time of the BB evolution in our simulations can be considered as the photochemical age (t_a) of BB aerosol evolving under idealized constant atmospheric conditions.

The optical properties of BB aerosol were simulated based on the Mie theory by using the OPTSIM software [57] which was combined with MDMOA earlier [57]. At each time step of the MDMOA simulation, OPTSIM received from MDMOA mass concentrations of all the model species in each size section. We assumed that BB aerosol particles are composed of a BC core surrounded by a shell composed of organic matter. The real and imaginary parts of the refractive index of BC were set at 1.95 and 0.79, respectively [1]. The organic shell was assumed to be nonabsorbing, that is, the contribution of brown carbon (BrC) to absorption was neglected. Available estimates of BrC absorption in Siberian BB plumes indicate that it is highly variable [49,58] but, on average, is rather weak within the visible wavelength range. Hence, the BrC absorption is unlikely to be a key factor determining the evolution of the radiative forcing efficiency of Siberian BB aerosol, although the impact of BrC on the radiative properties of Siberian BB aerosol needs yet to be clarified in future dedicated studies. The density of BB aerosol particles and the real refractive index of their organic shell were assumed to be 1.3 g/m^3 [16] and 1.55 [59], respectively. The OPTSIM output data included, in particular, values of the AOD, single scattering albedo (SSA), and asymmetry factor (AF) at 10 wavelengths ranging from 0.35–1.35 μm for each hour of the simulated BB aerosol evolution. The simulations analyzed below were performed with three initial concentrations of organic aerosol, C_0 , of 10, 50, and 100 $\mu\text{g}/\text{m}^3$ and three initial concentrations of BC/OA: 1.5, 3, and 6%. The simulations with the three different values of C_0 are henceforth referred to as c010, c050, c100. The simulated values of the optical properties of BB aerosol were used to compute the radiative effects of BB aerosol as explained below in Section 2.2.

2.2. Radiative Transfer Calculations

2.2.1. Radiative Transfer Code

We simulated the radiative effects of BB aerosol by using a multilayer horizontally homogeneous model of a clear-sky (cloudless) atmosphere (0–100 km). Within each layer, the dependence of the spectral optical aerosol characteristics (including the extinction coefficient σ_λ , single scattering albedo ω_λ , scattering phase function or asymmetry factor g_λ), molecular scattering coefficient $\sigma_{R,\lambda}$, as well as pressure, temperature, and concentration of

atmospheric gases on the altitude was disregarded. The effects of the underlying surface on the radiation were taken into account according to the Lambert law with albedo $A_{s,\lambda}$.

The broadband fluxes of solar radiation were calculated using a Monte Carlo radiative transfer code which we developed earlier [10,60,61]. Within this code, the downward (\downarrow) and upward (\uparrow) radiative fluxes at a given atmospheric level z are represented as a sum of fluxes in separate spectral intervals:

$$F^{\downarrow(\uparrow)}(z) = \sum_{i=1}^M F_i^{\downarrow(\uparrow)}(z), \quad (2)$$

where $M = 30$ is the number of bands $\Delta\lambda = (\lambda_i, \lambda_{i+1})$, $I = 1, \dots, M$, $\lambda_1 = 0.2 \mu\text{m}$, $\lambda_M = 5.0 \mu\text{m}$, including five bands in the UV, six in the visual, and 19 in the IR spectral ranges [62]. Within each band, the optical characteristics of aerosol and molecular scattering coefficient, as well as surface albedo, are assumed to be constant and equal to their values in the middle of the subinterval. The transmission function of the atmospheric gases within each band is approximated by a finite exponential series (correlated k-distribution method [63]) as in [48,64–66].

The radiative fluxes simulated with our radiative transfer code were previously found to be in satisfactory agreement with the results of line-by-line calculations [60,67] and data from field measurements [68,69]. In this study, the broadband radiative fluxes were calculated in the background and smoke-polluted atmosphere to estimate the ARF and ARFE of BB aerosol.

2.2.2. Input Parameters

Aerosol characteristics. Vertical profiles in the interval of 0–35 km and spectral variations in the optical characteristics of background aerosol were specified using a “continental average” model [70] that was designed to describe the typical aerosol optical characteristics under summer conditions in western Siberia [61]. The lower 2 km layer comprises water-soluble and water-insoluble fractions ($14 \mu\text{g}/\text{m}^3$ and $9.5 \mu\text{m}/\text{m}^3$ respectively), as well as black carbon ($0.5 \mu\text{m}/\text{m}^3$).

The radiative characteristics of the smoke-polluted atmosphere were computed assuming that BB aerosol occupies the layer of 0–1 km. The extinction coefficient, single scattering albedo, and asymmetry factor were calculated in the wavelength range of 0.35–1.35 μm at 10 wavelengths, as described in Section 2.1. To obtain a complete set of the input parameters for the radiative transfer simulations, the computations of the optical characteristics of BB aerosol were complemented as follows: (1) outside the interval of 0.35–1.35 μm , the extinction coefficient, single scattering albedo, and asymmetry factor were assumed to be constant and equal to the respective boundary values for $\lambda = 0.35 \mu\text{m}$ and $\lambda = 1.35 \mu\text{m}$; (2) within the layer of 0–1 km, SSA and AF of the “smoke + background” aerosol mixture were computed as a weighted average of the calculated values for the corresponding components, whereas AOD calculated for the smoke and background aerosols were summed up. Outside the smoke layer, the aerosol optical characteristics were assumed to be equal to those from the background aerosol model.

Molecular atmosphere. The transmission functions of the atmospheric gases were calculated based on the HITRAN2012 database and MT_CKD v.2.5 continuum model [71,72], using the regional model of temperature, pressure, and water vapor concentration profiles [73], developed for summer conditions of western Siberia and taking into account the absorption by all the atmospheric gases which were presented in the AFGL meteorological model [74]. The total water vapor content was assumed to be $2 \text{ g}/\text{cm}^2$, the total CO_2 content in the atmosphere was 400 ppm, and the total ozone content was set at 400 DU according to Aura OMI satellite data. (These values correspond to summer averages for the territory of western Siberia [75–77]).

The data of Fontenla et al. [78] were used for the extraterrestrial spectral solar radiance ($1367 \text{ W}/\text{m}^2$). The surface albedo corresponded to the albedo of the surface of the “mixed

forest" type [79]. The main calculations were performed for the solar zenith angle (SZA) of 35° , which roughly equals to midday Sun elevation on mid-summer at the latitude of Tomsk ($56^\circ 29'$). Therefore, our simulations are assumed to represent the dynamics of the atmospheric radiative fluxes due to gas-phase oxidation of BB OA within an idealized large-scale BB plume occupying the lowest 1 km-thick layer of the atmosphere under typical daytime conditions in Siberia in summer.

2.2.3. Simulated Radiative Properties

In this work, we consider instantaneous (for a given SZA) values of the radiative forcing of BB aerosol at the top and bottom of the atmosphere (TOA and BOA, respectively), as well as within the atmospheric column (ATM):

$$\Phi_{\text{TOA(BOA)}}(t) = F_{\text{TOA(BOA)}}^{\text{net,mix}}(t) - F_{\text{TOA(BOA)}}^{\text{net,bg}}(t), \quad (3)$$

$$\Phi_{\text{ATM}}(t) = \Phi_{\text{TOA}}(t) - \Phi_{\text{BOA}}(t), \quad (4)$$

where radiative influxes F^{net} at different levels are calculated as follows:

$$F_{\text{TOA(BOA)}}^{\text{net}}(t) = F_{\text{TOA(BOA)}}^{\downarrow}(t) - F_{\text{TOA(BOA)}}^{\uparrow}(t), \quad (5)$$

and the superscripts "mix" and "bg" correspond to the calculations in the smoke-polluted and background atmosphere respectively. The negative and positive values of $\Phi_{\text{TOA(BOA)}}$ are associated, respectively, with cooling and warming aerosol effects.

Using Equations (3) and (5), it is convenient to represent ARF values at the top and bottom of the atmosphere as follows:

$$\Phi_{\text{TOA}}(t) = F_{\text{TOA}}^{\uparrow,\text{bg}}(t) - F_{\text{TOA}}^{\uparrow,\text{mix}}(t), \quad (6)$$

$$\Phi_{\text{BOA}}(t) = (1 - A_s^*) \left(F_{\text{BOA}}^{\downarrow,\text{mix}}(t) - F_{\text{BOA}}^{\downarrow,\text{bg}}(t) \right), \quad (7)$$

where A_s^* is a certain effective value of the spectral albedo of the underlying surface in a given wavelength band.

Equations (6) and (7) can be used to qualitatively interpret the dependence of ARF on the aerosol optical characteristics, assuming that only one of them varies and all the others are kept constant (see also [80]):

- as AOD grows, $F_{\text{TOA}}^{\uparrow,\text{mix}}$ increases, while $F_{\text{BOA}}^{\downarrow,\text{mix}}$ decreases, so that Φ_{TOA} and Φ_{BOA} decrease (enhanced cooling effect);
- as SSA grows, $F_{\text{TOA}}^{\uparrow,\text{mix}}$ and $F_{\text{BOA}}^{\downarrow,\text{mix}}$ also grow and, consequently, Φ_{TOA} decreases, while Φ_{BOA} increases;
- as AF grows, the upward flux $F_{\text{TOA}}^{\uparrow,\text{mix}}$ decreases, while the downward flux $F_{\text{BOA}}^{\downarrow,\text{mix}}$ increases, so that Φ_{TOA} and Φ_{BOA} grow (warming effect).

Note that, when two or all three optical characteristics change simultaneously, they may have opposite effects on the radiative fluxes, so the response of ARF on these changes can only be predicted through numerical experiments.

While the ARF is strongly dependent on AOD (that is, on the extensive property of aerosol), the ARFE (Φ^e) is a useful characteristic to study the impact of the aerosol intrinsic properties (such as SSA and AF) on the radiative balance of the atmosphere. This characteristic is defined as a rate at which the atmosphere is forced per unit aerosol optical depth at $0.55 \mu\text{m}$ ($\tau_{0.55}(t)$):

$$\Phi_{\text{TOA(BOA)}}^e(t) = \Phi_{\text{TOA(BOA)}}(t) / \tau_{0.55}(t), \quad (8)$$

$$\Phi_{\text{ATM}}^e(t) = \Phi_{\text{ATM}}(t) / \tau_{0.55}(t). \quad (9)$$

It should be kept in mind that ARFE is still not fully independent of the aerosol load because multiple scattering effects and attenuation of the transmitted radiation introduce nonlinearity into the dependence of ARF on AOD [81]. The units for ARFE are $W/(m^2\tau)$; increased radiative forcing efficiency means the increased absolute value of Φ^e .

3. Results

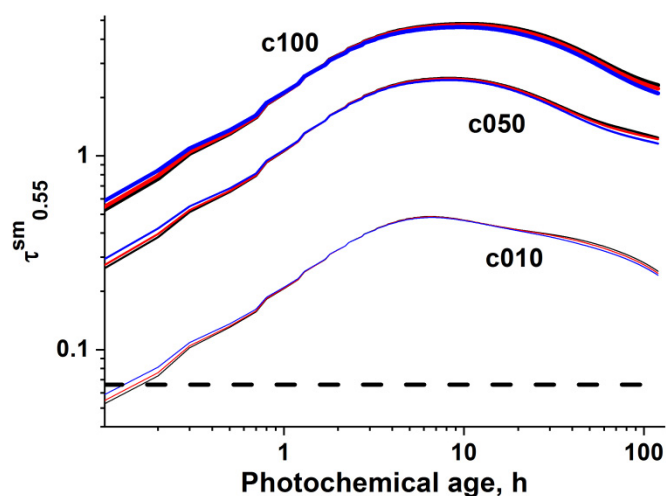
3.1. Dynamics of the Optical Characteristics of BB Aerosol

This section describes the key features of the simulated evolution of the optical properties of BB aerosol. For definiteness, all the values are reported below for the 0.55 μm wavelength.

The time evolution of AOD and SSA (see Figure 1a,b) can be separated into two distinct stages. At the first stage, both characteristics rapidly increase to maximal values during the first 7–10 h ($0 \leq t \leq t_{\text{max}}$), with the most intense growth in the first hour. Then, at the second stage ($t \geq t_{\text{max}}$), they slowly (compared to the growth rate) decrease. For instance, AOD of BB aerosol ($\tau_{0.55}^{\text{sm}}(t)$), calculated with $C_0 = 10 \mu\text{g}/\text{m}^3$ (almost irrespectively of the BC/OA ratio), increases in ~ 7 h from 0.057 to 0.48, decreasing to 0.24 at the end of this interval ($t = 120$ h); while $\tau_{0.55}^{\text{sm}}(t)$ obtained with $C_0 = 100 \mu\text{g}/\text{m}^3$ increases from 0.54 to 4.7 in the first ~ 10 h and decreases afterward to 2.2. Note that for a fixed initial concentration OA in this BC/OA variability range, $\tau_{0.55}^{\text{sm}}(t)$ varies just within ~ 1 –2%, reflecting the fact that BC contributes only very insignificantly to the BB aerosol mass concentration (and, thus, to its extinction cross-section).

The simulated dynamics of AOD is qualitatively similar to the dynamics of BB OA mass concentration, which was calculated using MDMOA with the K21 scheme previously [34]. The reasons for such non-monotonic behavior of BB OA mass concentration are discussed in detail elsewhere [34]. Briefly, initial oxidation of VOCs and POA in functionalization reactions results in the rapid formation of SOA, which is then getting more slowly oxidized in fragmentation reactions leading to an eventual decrease of the OA concentration. The same processes account for the nonmonotonous evolution of SSA (Figure 1b). Specifically, the increase in SSA (at the first stage of the evolution) is due to a decrease in the BC/OA ratio as a result of SOA formation [34], and the following slow decrease of SSA is a result of degradation and evaporation of both POA and SOA.

The widest variability range of SSA of organic aerosol ($\omega_{0.55}^{\text{sm}}(t)$) is observed for a high initial value of BC/OA (6%), when the single scattering albedo first increases from ~ 0.8 to ~ 0.97 , then slightly decreases (by ~ 0.02) towards the end of the simulation period of 120 h. At BC/OA = 1.5%, the variations of $\omega_{0.55}^{\text{sm}}(t)$ do not go beyond the interval of 0.94–0.99, indicating that the effect of SOA formation on the aerosol scattering properties diminishes with decreasing BC/OA ratio.



(a)

Figure 1. Cont.

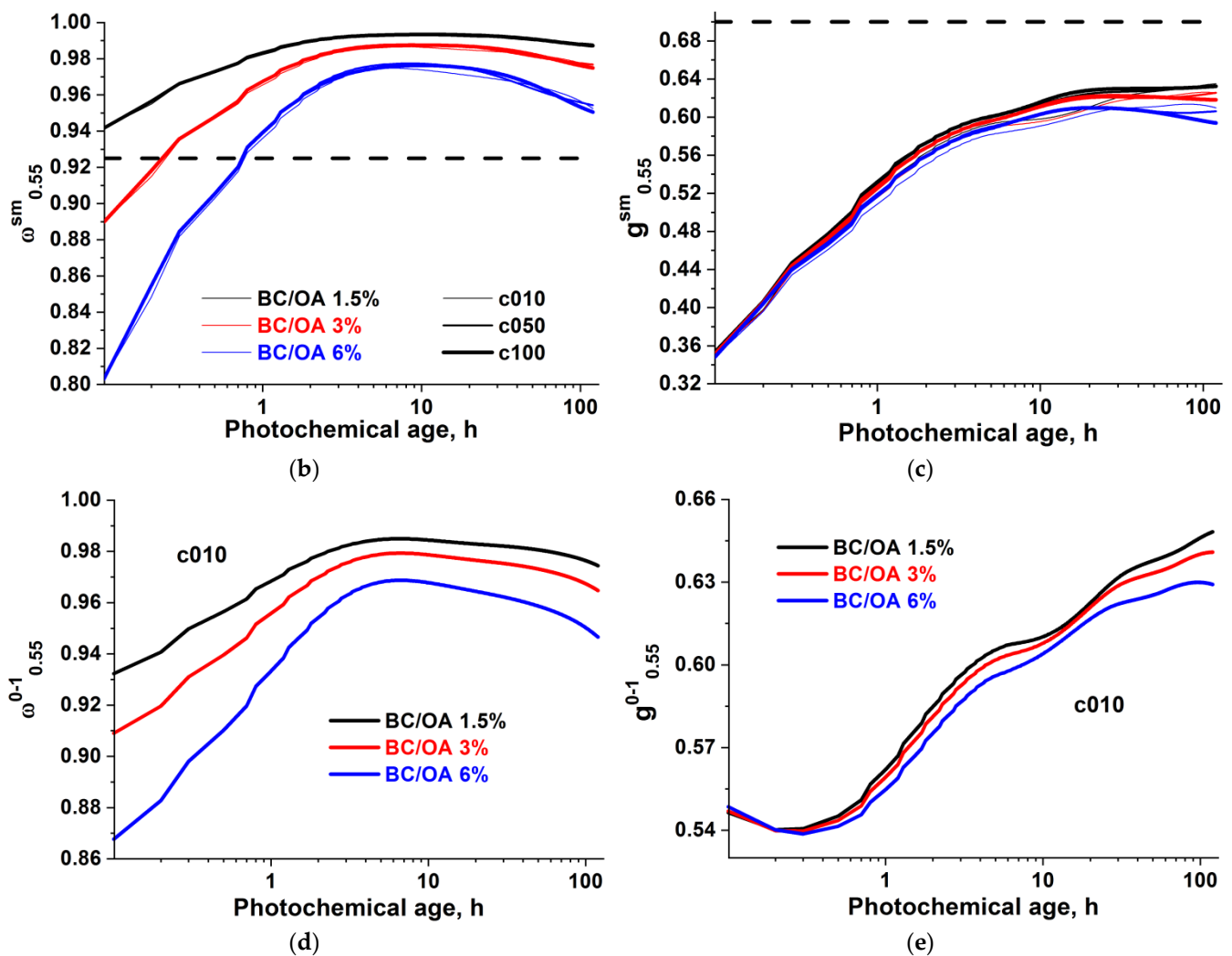


Figure 1. Simulated dynamics of the optical characteristics of BB aerosol: (a) AOD, (b) SSA, and (c) AF for different initial OA concentrations and BC/OA ratios. Straight dash horizontal lines indicate the corresponding optical characteristics of background aerosol in the bottom layer of 0–1 km. The optical characteristics in the “smoke+background” mixture with the initial concentration c010 in the layer of 0–1 km (d) SSA ($\omega_{0.55}^{0-1}$), (e) AF ($g_{0.55}^{0-1}$).

Similar to AOD and SSA, the asymmetry factor of OA significantly increases at the initial stage of the evolution: specifically, $g_{0.55}^{sm}(t)$ increases considerably, from ~ 0.36 to ~ 0.60 – 0.62 , in the period from $t = 0$ to $t \sim 7$ – 10 h, depending on initial concentration OA and the BC/OA ratio rather weakly (Figure 1c). At the second stage, it remains nearly constant. These changes in AF are likely driven by the evolution of the size distribution of BB aerosol particles. According to our simulations, rapid formation and condensation of secondary organic compounds at the first stage results in a rapid decrease of the volume fraction of the particles with a diameter less than $0.2 \mu\text{m}$. This decrease is a likely reason for the rapid growth of AF at this stage. At the second stage, volatilization of the SOA components due to the fragmentation process results in a decrease of the fraction of particles with a diameter of about $0.3 \mu\text{m}$ but the effect of this decrease on AF is partly compensated by the increase of the fraction of the more slowly evaporating particles with the diameter bigger than $0.6 \mu\text{m}$.

The results presented above address the optical properties of aerosol in only the lowest 1 km layer in our radiative transfer model, depending on initial OA concentration and the BC/OA ratio rather weakly while the solar radiative fluxes form within the entire atmospheric column. With initial OA concentrations of 50 and $100 \mu\text{g}/\text{m}^3$, the optical depth of the smoke layer is about a factor of 5–40 larger than AOD values under the

background conditions $\tau_{0.55}^{\text{bg}}(t)$ (Figure 1a); therefore, the effect of the optical characteristics of background aerosol on AOD, SSA, and AF is barely manifested in both lower layer and the atmospheric column. However, at the beginning of the c010 simulation, the background, and smoke aerosol depths are comparable, so that SSA and AF of smoke ($\omega_{0.55}^{\text{sm}}(t)$ and $g_{0.55}^{\text{sm}}(t)$) and “smoke + background” mixture ($\omega_{0.55}^{0-1}(t)$ and $g_{0.55}^{0-1}(t)$) can strongly differ. In particular, with BC/OA = 6% at the initial time ($t = 0$), SSA increases from 0.8 to 0.87 (Figure 1b,d); while AF increases from ~ 0.36 to 0.54 and changes little during the first hour (Figure 1c,e), independent of the ratio BC/OA. Note that possible nonlinearities in the evolution of BB aerosol due to the dependence of the gas-phase concentration of SVOCs on the OA concentration (see Equation (1)) turned out to be quite insignificant within a rather limited range of C_0 values considered in our simulations reported here. This fact simplifies the interpretation of the results of our numerical experiments. A much stronger impact of the initial concentration on the BB aerosol evolutions can be expected in the simulations covering a much larger range of possible values of C_0 and taking into account the dilution process [46].

3.2. Radiative Forcing

Figure 2 demonstrates the simulated evolution of the ARF at both top and bottom of the atmosphere. The results indicate (Figure 2a) that the cooling effect of BB aerosol is more strongly manifested at the BOA level than at the TOA level ($|\Phi_{\text{BOA}}(t)| > |\Phi_{\text{TOA}}(t)|$), but increases with an increase of the initial OA concentration at both levels (see also [48]). Not surprisingly, the time variations of $|\Phi_{\text{BOA(TOA)}}(t)|$ follow those of $\tau_{0.55}(t)$ (Figure 1): an increase (decrease) in $\tau_{0.55}(t)$ entails an increase (decrease) of the absolute value of the ARF at both top and bottom of the atmosphere. However, whereas with c050 and c100, a larger amplitude of the $\Phi_{\text{BOA(TOA)}}(t)$ variations corresponds to stronger AOD variations in the first time interval as compared to the second interval, the ARF variability ranges for $0 \leq t \leq t_{\text{max}}$ and $t_{\text{max}} \leq t \leq 120$ h are almost the same (but very small) with c010. This indicates that, for small concentrations of OA, the formation of ARF is influenced not only by AOD but also by SSA and AF.

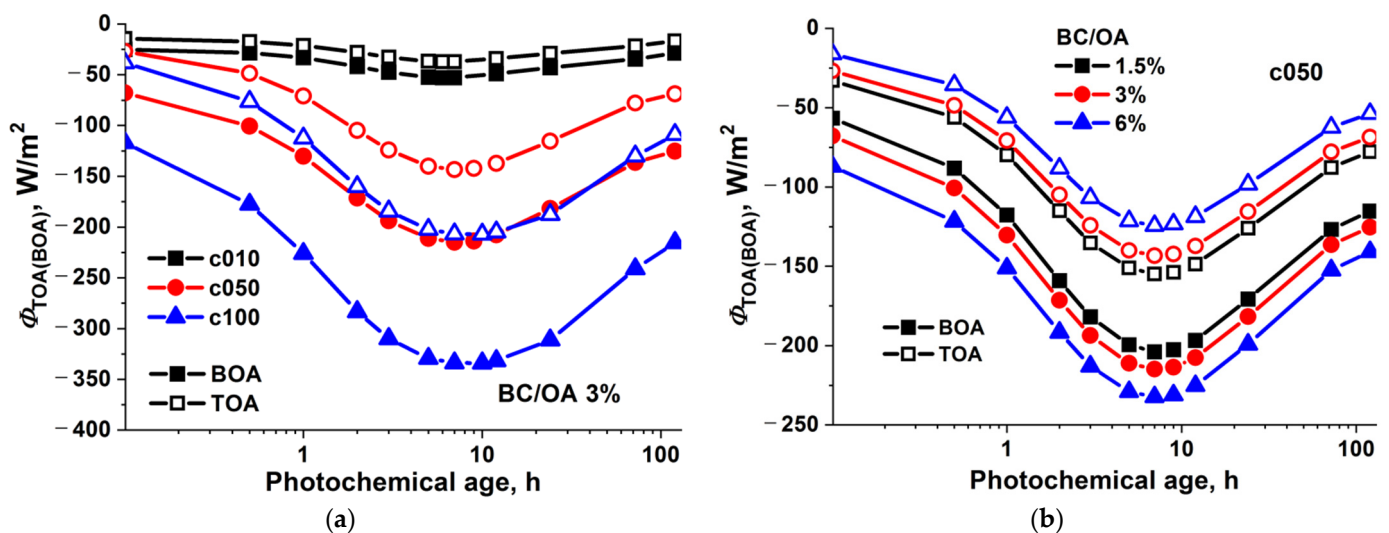


Figure 2. Aerosol radiative forcing at the top and bottom of the atmosphere (a) for different concentrations OA with the initial value of the BC/OA ratio equal to 3% and (b) for different relative BC/OA contents with c050. The lines with hollow and solid symbols correspond to the aerosol forcing estimates at the top and bottom of the atmosphere (TOA and BOA), respectively.

It is also not surprising that an increase in the absorption by aerosol particles leads to a decrease in the absolute value of the negative ARF at TOA, but it is worth noting that the stronger absorption increases the cooling at BOA (Figure 2b). The comparison

of results shows how strongly the amplitude of ARF variations depends on the aerosol absorbing properties. For instance, in the time interval $0 \leq t \leq t_{\max}$ in the case of weakly absorbing aerosol ($BC/OA = 1.5\%$), the $\Phi_{TOA}(t)$ value varies by a factor of ~ 4.8 (from -32 to -154 W/m^2); while with $BC/OA = 6\%$, $\Phi_{TOA}(t)$ decreases from -16 to -124 W/m^2 , i.e., by about a factor of 7.8 (Figure 2b).

The quantitative estimates of ARF presented in Figure 2 are consistent with the results obtained by other authors for extreme biomass-burning events in the Arctic and central Russia (e.g., [82–84]).

We conclude this subsection by presenting examples of the atmospheric radiative forcing calculations (Figure 3). The $\Phi_{ATM}(t)$ value characterizes the changes of the absorption P in the atmospheric column when going from the background ($P^{bg}(t)$) to the smoke-polluted conditions ($P^{mix}(t)$). Considering that $P^{bg}(t)$ is a certain constant value determined by the background atmospheric state, the $\Phi_{ATM}(t)$ evolution depends exclusively on time variations in $P^{mix}(t)$ which, in turn, is determined by time variations in AOD and SSA. From general considerations, it follows that an increase in AOD with SSA kept fixed favors $\Phi_{ATM}(t)$ increase due to the growing number of interactions of photons with particles in the atmosphere; at the same time, an SSA growth for fixed AOD means a decrease of $\Phi_{ATM}(t)$. If AOD and SSA increase simultaneously, the factors indicated above have opposite effects on P , which either increases or decreases, depending on which of the factors dominates.

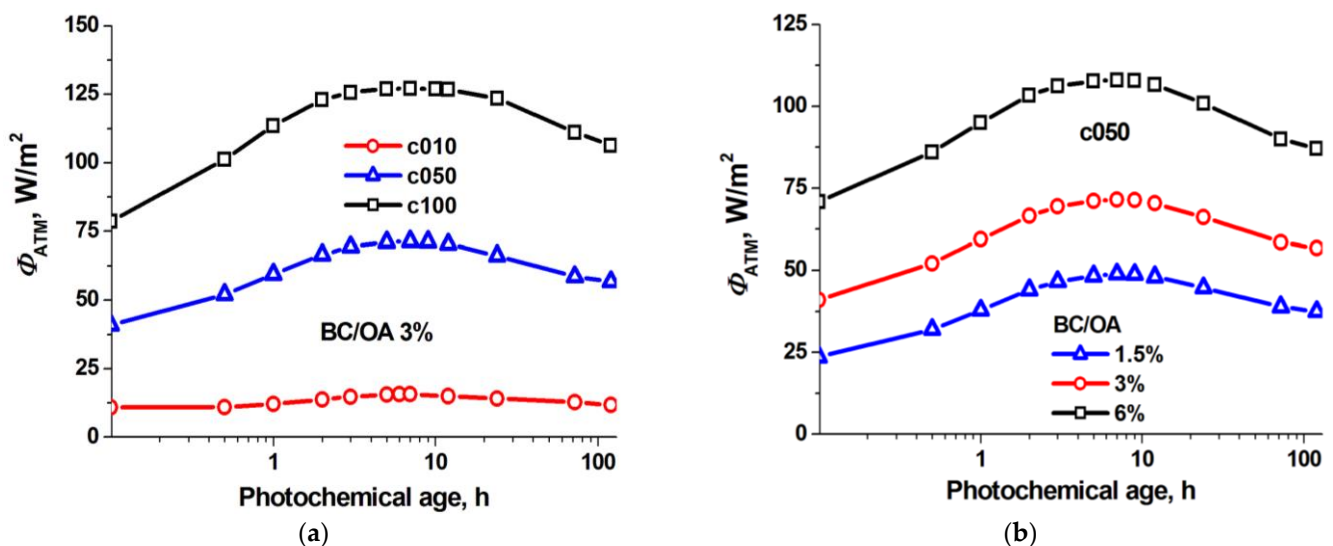


Figure 3. Radiative forcing of the atmosphere (a) for different concentrations OA with BC/OA ratio equal to 3% and (b) for different relative BC/OA contents with c050.

For a fixed initial BC/OA ratio, the time variations in $\Phi_{ATM}(t)$ correlate with changes in the aerosol optical depth of the atmosphere: $\Phi_{ATM}(t)$ increases in the first 7–10 h and decreases for $t \geq t_{\max}$ for all initial concentrations OA (see Figures 1a and 3a). Note that although the $\Phi_{ATM}(t)$ variations in the case with a low initial OA concentration (c010) are manifested much weaker than in cases c050 and c100, the relative increase of $\Phi_{ATM}(t)$ is significant (a factor of ~ 1.5). Not surprisingly, for a fixed initial concentration OA, the evolution of $\Phi_{ATM}(t)$ is determined by both time variations in AOD (consistent with results in Figure 3a), and by variations in the absorption cross-section of aerosol particles: the bigger AOD and the BC/OA ratio, the greater the $\Phi_{ATM}(t)$ value.

Some of the results above (e.g., nonproportional ARF and AOD variations for a fixed aerosol absorption), obtained from a detailed analysis, indicate that the formation of aerosol radiative forcing may be influenced not only by AOD evolution but also by time variations in aerosol scattering and absorbing properties, as was already pointed out before by other authors [48,81–89].

3.3. Radiative Forcing Efficiency

To identify the tendencies caused by variations in SSA and AF under the fixed atmospheric conditions and surface parameters, we will study the evolution of the aerosol radiative forcing efficiency (ARFE), which, within a rough approximation, is independent of AOD.

Bottom of the atmosphere. In the period $0 \leq t \leq t_{\max}$, ARFE at BOA, $\Phi_{\text{BOA}}^e(t)$, decreases with time in the absolute value, irrespectively of values of C_0 and the BC/OA ratio (Figure 4a). This is because SSA and AF increase in the initial time interval (Figure 1b,c), so that the effect of surface warming intensifies, i.e., $|\Phi_{\text{BOA}}^e(t)|$ decreases. Note that the behavior of $\Phi_{\text{BOA}}^e(t)$ with c050 is not shown in Figure 4a, being qualitatively similar to that with c100. As the aerosol evolution proceeds ($t > t_{\max}$), the $|\Phi_{\text{BOA}}^e(t)|$ value continues decreasing for c010, but with c050 and c100, $|\Phi_{\text{BOA}}^e(t)|$ increases. Possibly, this is because the behavior of $\Phi_{\text{BOA}}^e(t)$ for small concentrations of OA is driven mostly by the behavior of the asymmetry factor. However, the increase in C_0 enhances the effect of the SSA variations, which results in the growth of ARFE (consistent with results in [48,80,81]).

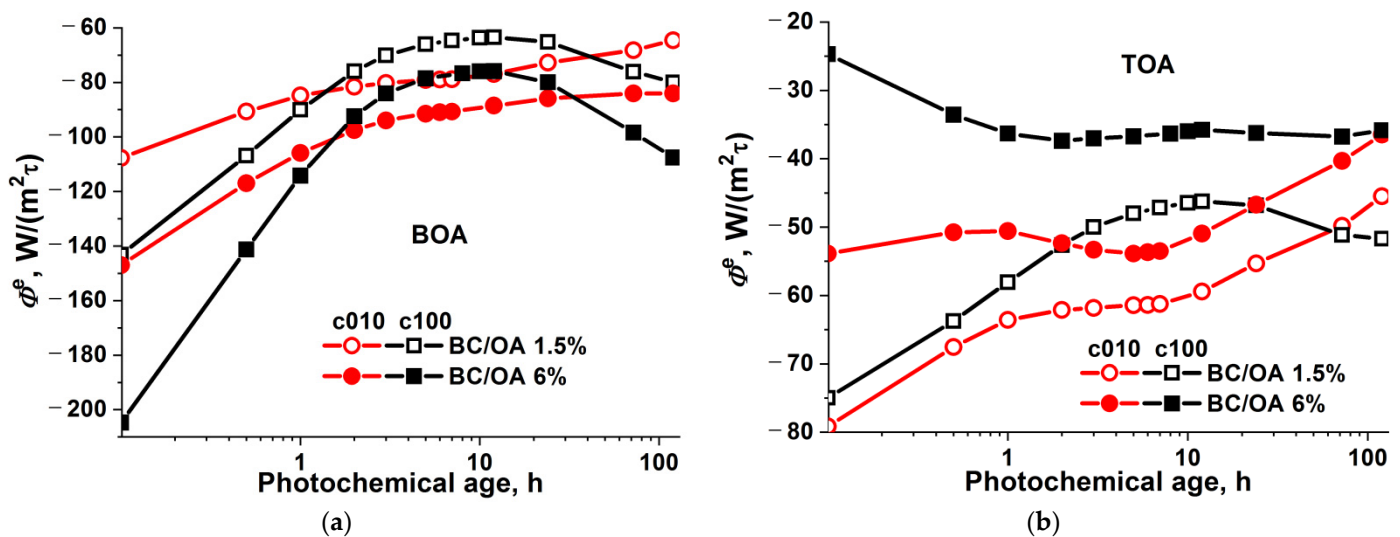


Figure 4. The aerosol radiative forcing efficiency at the bottom (a) and top (b) of the atmosphere according to calculations with different values of C_0 and the BC/OA ratio.

For all of the initial OA concentrations, the change in the $|\Phi_{\text{BOA}}^e(t)|$ shows a larger amplitude of the variation in the period $0 \leq t \leq t_{\max}$ as compared to the subsequent period $t > t_{\max}$, with the value of the amplitude being maximal when the BC/OA ratio equals to 6% because the SSA variability ranges for BC/OA = 1.5 and 3% are smaller than with BC/OA = 6% at the initial evolution stage. In the second time interval, the amplitudes of the SSA variations strongly decrease as compared to the first 7–10 h (Figure 1b,d).

Top of the atmosphere. The radiative forcing efficiency is smaller (in the absolute value) at the top than at the bottom of the atmosphere ($|\Phi_{\text{TOA}}^e(t)| < |\Phi_{\text{BOA}}^e(t)|$, Figure 4). As the absorption by aerosol particles increases (with an increase of BC/OA), $|\Phi_{\text{TOA}}^e(t)|$ decreases. This is because an SSA decrease reduces the energy available to be backscattered towards the TOA and into the space (an analogous result was found in other studies, e.g., [48,88]).

For a low initial concentration (c010), the $|\Phi_{\text{TOA}}^e(t)|$ value decreases during the entire period of the evolution when the initial concentration BC/OA = 1.5% (Figure 4b). This decrease is driven by the increase of the $g_{0.55}^{0-1}(t)$, which turns out to be a more important factor compared to variations in $\omega_{0.55}^{0-1}(t)$ (Figure 1d,e). As the absorption increases (BC/OA = 6%), the opposite effects of enhancements in $\omega_{0.55}^{0-1}(t)$ and $g_{0.55}^{0-1}(t)$ on ARFE tend to cancel each other out (see also [88]), yielding a slightly varying value of $\Phi_{\text{TOA}}^e(t)$ for $0 \leq t \leq t_{\max}$. The following decrease in $|\Phi_{\text{TOA}}^e(t)|$ is due to the warming effect owing to the combined action of an increase in $g_{0.55}^{0-1}(t)$ and a slight decrease in $\omega_{0.55}^{0-1}(t)$ (Figure 1d,e).

In the c100 simulation, the SSA and AF effects on $\Phi_{\text{TOA}}^e(t)$ are mitigated as multiple scattering effects play an increasingly important role when AOD is large. Nonetheless, distinctive changes in the ARFE due to changes in SSA and AF can still be identified. In particular, during the period of $0 \leq t \leq t_{\text{max}}$, $|\Phi_{\text{TOA}}^e(t)|$ decreases for BC/OA = 1.5% (Figure 4b) because $g_{0.55}(t)$ grows with time (Figure 1c). With an increasing range of the variability in $\omega_{0.55}(t)$ in the simulation with BC/OA = 6%, the TOA cooling (that is, an increase in $|\Phi_{\text{TOA}}^e(t)|$) is mostly determined by the evolution of SSA.

Analysis of the evolution of the absorption forcing efficiency in the atmospheric column ($\Phi_{\text{ATM}}^e(t)$) shows (Figure 5) that being weakly dependent on AOD (by definition) $\Phi_{\text{ATM}}^e(t)$ matches the SSA variations in time (as the absorption by aerosol particles decreases/increases, $\Phi_{\text{TOA}}^e(t)$ decreases/increases, as in [10]). The minimal value of $\Phi_{\text{ATM}}^e(t)$ and its narrowest variability range are observed in the c010 simulation, irrespectively of BC/OA. This is because the difference in the absorption between the background and smoke-polluted atmospheres is observed for a minimal initial OA concentration from the range considered here (c010, Figure 3a). We also note that, independently of BC/OA, the $\Phi_{\text{ATM}}^e(t)$ values with c050 and c100 differ most strongly at the beginning of the evolution process, seemingly due to the strong difference in SSA, and then become closer in magnitude as the magnitude of the difference in the SSA values for the different cases becomes smaller (Figure 1b).

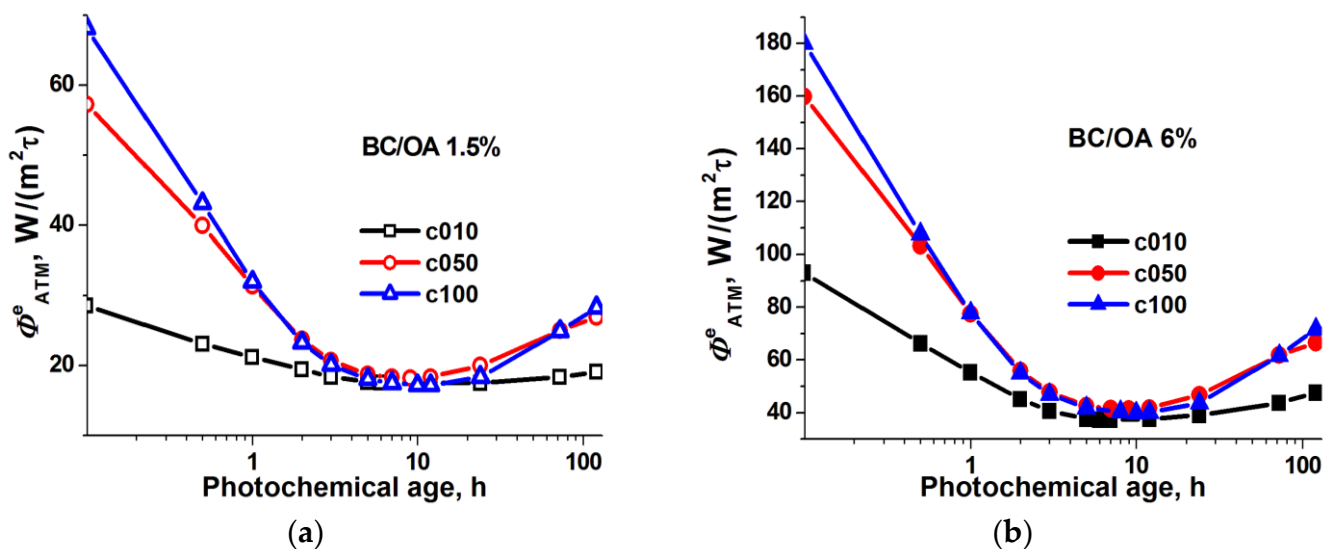


Figure 5. The effective radiative forcing of the atmosphere, calculated for different values of C_0 with the initial value of the BC/OA ratio equal to (a) 1.5% and (b) 6%.

4. Discussion

In this section, we would like to highlight the key findings from our analysis and discuss their possible implications for other modeling studies of the radiative effects of BB aerosol. We will also briefly discuss the limitations of our analysis.

One of our most important findings is that the radiative forcing efficiency of BB aerosol at TOA (Φ_{TOA}^e) is not significantly affected by the OA oxidation processes. More specifically, the changes in the intensive optical properties (SSA and AF) of BB aerosol, which occur as a result of the OA transformations due to the oxidation processes and can be very profound according to both our simulations and available observations [14,32,34], are not found to have a major impact on Φ_{TOA}^e . As noted above (Section 3.2), this result can be explained by a partial compensation of the opposite effects of, on the one hand, an increase (decrease) in SSA and, on the other hand, an increase (decrease) in AF and an enhancement (diminishing) of the role of the multiple scattering. Accordingly, it seems reasonable to expect, that the evolution of the ARF by real large-scale BB plumes is very closely associated with the evolution of AOD, at

least when it is possible to disregard the BB aerosol aging processes which were not addressed in our analysis (such as deposition, coagulation, humidification of particles, and changes in the BrC absorption). In other words, our result indicates that AOD can be used as a good proxy for studying the impact of the OA evolution on the ARF, as was suggested earlier [45], and that the focus in the validation of the representation of BB organic aerosol evolution in models of various complexities should be given to comparing the simulated and modeled evolution of AOD (as was done in our previous studies [33,34]). However, as a caveat, it should be noted that since our box model simulations are designed to be representative of the evolution of only large-scale BB plumes originating from Siberian fires, the above does not necessarily mean that an effect of the changes in the intensive optical properties of aging BB aerosol on the evolution of the ARFE at TOA is always quantitatively negligible, irrespective of the region of the world and the fire size. It should also be noted that although the Φ_{TOA}^e does not change considerably as a result of BB aerosol aging in our simulations, it can significantly (by a factor of two or more) differ for different initial OA concentrations, mainly as a manifestation of the effect of the multiple scattering. Hence, assuming a fixed linear relationship between AOD and Φ_{TOA}^e would not always be correct.

We also found that changes in the intensive optical properties of BB aerosol can make a considerable impact on the evolution of ARF at both the bottom of the atmosphere and within the atmospheric column (Φ_{BOA} and Φ_{ATM}), as evidenced, in particular, by strong variations in the corresponding values of ARFE (Φ_{BOA}^e and Φ_{ATM}^e). Consistent with these variations, the maximum changes in both Φ_{BOA} and Φ_{ATM} are found to be several times smaller than those in the variations of AOD. Furthermore, variations in Φ_{BOA}^e and Φ_{ATM}^e are found to be strongly sensitive both to the BC/OA ratio and the initial concentration of OA (C_0). In particular, an increase in C_0 not only strongly enhances the variations in both Φ_{BOA}^e and Φ_{ATM}^e but also results in qualitative changes in the evolution of Φ_{BOA}^e , leading to the nonmonotonous behavior of this characteristic with $C_0 = 100 \mu\text{g}/\text{m}^3$ instead of the monotonous growth with $C_0 = 10 \mu\text{g}/\text{m}^3$. Interestingly, the dependencies of the Φ_{BOA}^e and Φ_{ATM}^e on C_0 are practically not associated with the intrinsic nonlinearity of the OA system [44,46] but are rather a manifestation of the nonlinearity of the relationship between the atmospheric load of BB aerosol and its radiative properties due to the multiple scattering on the radiative fluxes. We believe that these findings contribute to the fundamental understanding of the impact of OA evolutions on the radiative and climate impacts of BB aerosol.

A more practical aspect of our results concerns possible biases in simulations of the BB radiative effects using 3D models of various complexities. Specifically, if the OA evolution is disregarded in a model, and the aerosol optical properties correspond to those of fresh aerosol, both Φ_{BOA}^e and Φ_{ATM}^e will likely be overestimated in absolute value in a region (such as the Arctic) dominated by aged BB aerosol (presuming that the simulated AOD agrees with the corresponding observations in the region), leading to either a negative bias in the surface temperature due to too strong cooling of the surface or a positive bias in it due to too strong heating of the near-surface air. Note that although Φ_{BOA} and Φ_{ATM} are less frequently reported in the literature than Φ_{TOA} , they are nevertheless important factors in the context of the regional climate impacts of aerosol, and as such have been estimated for various types of aerosol in many studies [10,48,90–93].

We would like to emphasize that this paper presents the first experience of an in-detail modeling study of the effects of the atmospheric transformation of the organic component of BB aerosol on the radiative forcing of OA and its efficiency. The results of this study have a qualitative (rather than quantitative) character, which is an inevitable consequence of using a box model. This kind of model is not expected to ensure quantitatively accurate representation of the complex atmospheric processes. However, a box model is an indispensable tool when the task is to entangle intertwined effects of the multiple processes driving the atmospheric evolution of BB aerosol [44–46,94]. Ultimately, results of the box model analysis can provide a better understanding of the contribution of individual factors to the radiative effects of BB aerosol and can guide planning and interpretation of dedicated field studies [21,45]. Note that deducing the differences between the radiative effects of BB

aerosol of the different ages directly from observations is possible but challenging particularly because of the strong variability of the optical properties of BB aerosol originating from different fires [95].

It should be kept in mind that this study is limited by consideration of only the ARF changes that can occur as a result of the OA oxidation processes. At the time scale of several days, the evolution of the optical and radiative properties of BB aerosol can be significantly affected by other processes, such as dilution, coagulation, and deposition. In particular, dilution is likely to result in faster evaporation of both POA and SOA components from the particles [44,46], leading to a shift of the accumulation mode to smaller particles and an increase of the BC/OA ratio. The exact effects of these changes on the ARF are difficult to predict but most likely they will counteract the changes associated with the formation of SOA. Conversely, the coagulation effect will likely be manifested in the increase of both SSA and AF (as a result of a shift of the size distribution to bigger particles [14,96]). We also expect that dry deposition does not have a significant impact on ARFE, since it is likely to mostly affect coarse particles [97] at the time scale considered, which do not contribute significantly to the optical properties of BB aerosol at the UV and visible range [98].

Finally, it should also be noted that our simulations of the OA evolution were performed using a highly simplified VBS scheme. The main advantage of this scheme is that it was shown [34] to adequately reproduce the evolution of some key optical properties of a large-scale plume originating from Siberian fires, including AOD at 550 nm and SSA at 388 nm. However, the simplified character of this scheme means that the assumed simplified representation of the oxidation processes can compensate for some effects which are not taken into account in our simulations, including the effects of the transition of the phase state of OA particles [98], particle viscosity [99], inhomogeneous mixing of the organic solutions [100], and SOA photolysis [101]. The role of these effects in the evolution of BB aerosol and its optical and radiative properties is presently poorly known, especially in Siberia, and should be clarified in future studies. Further studies are needed to examine possible changes in the evolution of the ARFE due to BrC absorption [49,102,103] which has also been disregarded in the simulation presented in this paper.

5. Conclusions

In this paper, we presented the results of the numerical analysis of the changes in the radiative forcing of BB aerosol due to the atmospheric photochemical aging of its organic component. The analysis was based on simulations performed using a microphysical box model [46], a Mie code [57], and a radiative transfer code [60].

The photochemical evolution of BB OA was simulated for a 120 h interval by using a simplified VBS scheme which was introduced in a previous study [34]. In this scheme, primary and secondary SVOCs are split respectively into two and three volatility classes whose chemical evolution is driven by oxidation reactions with the hydroxyl radical. It takes into account the formation of secondary organic aerosol as a result of the oxidation of volatile organic compounds (VOCs) and primary semivolatile components of organic aerosol (POA). The key advantage of this scheme is that it was shown (using satellite observations) to adequately reproduce the multiday atmospheric evolution of AOD in BB plumes originating from forest fires in Siberia [34]. Given the focus of this study on the effects of oxidation processes on the BB aerosol radiative properties, we disregarded coagulation and deposition of the particles. We also disregarded dilution, as our analysis was restricted by an idealized limiting case of BB plumes from large-scale fires, for which the dilution is very slow.

The optical properties (AOD, SSA, and AF) of BB aerosol were computed for three initial values of the OA mass concentration ($C_0 = 10, 50, \text{ and } 100 \mu\text{g}/\text{m}^3$) and three initial values of the mass ratio of BC and OA ($\text{BC}/\text{OA} = 1.5, 3, \text{ and } 6\%$), which were intended to cover a considerable part of the range of variability of these parameters in Siberian BB plumes. Qualitatively consistent with previous 3D model simulations of the evolution of AOD in Siberian BB plumes [34], our box model simulations demonstrated a rapid

increase in AOD during the initial 7–10 h, followed by a much slower decrease. Such nonmonotonous AOD behavior is due to the rapid formation of SOA as a result of oxidation of VOCs and POA and consecutive volatilization of part of SOA as a result of fragmentation reactions. Since the formation and volatilization/degradation of SOA are associated with variations of the BC/OA ratio, the same factors were the drivers of the rapid increase and slower decrease in SSA (which is mostly determined by the BC/OA ratio) at the initial and later stages of the simulations, respectively. The asymmetry factor, which is mostly controlled by the particle size distribution, is also found to initially enhance with time, but its dependence on the aerosol photochemical age becomes close to neutral after 7–10 h.

Our calculations of the broadband fluxes (0.2–5 μm) in the background atmosphere were carried on the base of a “continental average” model [70] that was designed to represent the typical aerosol optical characteristics under summer conditions in western Siberia [61]. The same model was used for the computation of the radiative characteristics of the smoke-polluted atmosphere, assuming that BB aerosol occupies the 1 km-thick lowest layer of the atmosphere.

With the assumed values for the characteristics of atmosphere and the underlying surface (moderate values of SSA for the background aerosol and relatively low albedo of the underlying surface), the BB aerosol is found to have a cooling effect at both top and bottom of the atmosphere (TOA and BOA). The cooling effect is more pronounced at BOA than at TOA. As could be expected, variations in the aerosol radiative forcing (ARF) are closely related to those in AOD. The ARF (negative) at both boundaries of the atmosphere increases (that is, it becomes smaller by the absolute value) or decreases as a result of a decrease or an increase in the BB aerosol loading, respectively, whereas the ARF (positive) in the atmospheric column demonstrates an increasing dependence on AOD.

To analyze the effects of the scattering and absorption properties of BB aerosol on its radiative forcing, we considered the ARF efficiency (ARFE) that is defined as the ratio of the ARF to AOD. The dependence of ARFE on the BB aerosol photochemical age is found to be complex, being formed under the effect of variations in both SSA and AF. The effects of these factors either compete (at the top of the atmosphere) or reinforce each other (at the bottom of the atmosphere). Specifically, an increase in SSA intensifies or diminishes the cooling at TOA and BOA levels, respectively, whereas an increase in AF diminishes the cooling, also at both TOA and BOA. An increase in AOD tends to dampen the effects of SSA and AF due to an enhancement in the multiple scattering effects.

The results of our simulations also indicate that the ARFE is sensitive to the initial values of both OA concentration (C_0) and the BC/OA ratio.

- At the bottom of the atmosphere, the $\Phi_{\text{BOA}}^e(t)$ increases (that is, its absolute value becomes less) during the entire evolution process when C_0 is small ($10 \mu\text{g}/\text{m}^3$), which is mostly due to the dominant role of the asymmetry factor whose growth leads to an increase in the downward radiation fluxes. With much larger initial aerosol concentration increases ($C_0 = 100 \mu\text{g}/\text{m}^3$), the $\Phi_{\text{BOA}}^e(t)$ still initially increases but decreases at the second stage of the evolution;
- At the top of the atmosphere, the $\Phi_{\text{TOA}}^e(t)$ increases (decreases by the absolute value) for the entire period of the simulation with the lowest C_0 and BC/OA values due to the predominant influence of the changes in AF. As the BC/OA ratio increases, the competing effects of SSA and AF tend to compensate each other, resulting in a weaker dependence of ARFE on the photochemical age. An increase in the initial OA concentration up to $C_0 = 100 \mu\text{g}/\text{m}^3$ results in a more complex dependence of the ARFE on SSA and AF becomes due to the stronger effects of multiple scattering;
- The dependence of the ARFE in the atmospheric column on the OA photochemical age is mirroring the corresponding dependence (taken with an opposite sign) of SSA: that is, the ARFE decreases or increases with an increase or decrease of SSA.

It should be noted that the radiative fluxes reported in this paper were calculated assuming constant characteristics of the atmosphere (except for those of BB aerosol) and the underlying surface (mixed forest), as well as the solar zenith angle ($\text{SZA} = 35^\circ$ at noon on

mid-summer at the latitude of Tomsk). Addressing a wider range of SZA and underlying surface types, as well as accounting for the variety of atmospheric situations is likely to entail some changes in the revealed regularities in the ARF and ARFE evolution. These possible changes will need to be identified in future studies. In addition, the use of more complex (chemically speciated) representations of the photochemical evolution of BB OA in future studies is needed to clarify the role of actual organic components in the evolution of the radiative effects of BB aerosol. Finally, we would like to emphasize that this study was focused on the analysis of only daytime evolution of the radiative forcing of BB aerosol due to gas-phase oxidation processes. Possible effects of other processes underlying the atmospheric aging of BB aerosol on the ARF and ARFE evolution should be addressed in dedicated studies.

Author Contributions: Conceptualization, T.B.Z. and I.B.K.; calculation, I.M.N. and N.A.G.; analysis of results, T.B.Z., I.B.K., I.M.N. and M.B.; writing—original draft preparation, T.B.Z. and I.B.K.; writing—review and editing, T.B.Z., I.B.K., I.M.N. and M.B. All authors have read and agreed to the published version of the manuscript.

Funding: The analysis of the evolution of the radiative effects of BB aerosol was funded by RFBR and CNRS according to the research project № 21-55-15009; the preparation of input parameters and the algorithm modifications for radiation computations were performed in the framework of the state assignment of the Institute of Atmospheric Optics, Siberian Branch, Russian Academy of Sciences, Tomsk; the simulations of the OA aerosol evolution were performed in the framework of the state assignment № 0030-2021-0008 of the Institute of Applied Physics, Russian Academy of Sciences, Nizhny Novgorod.

Institutional Review Board Statement: Not applicable.

Informed Consent Statement: Not applicable.

Conflicts of Interest: The authors declare no conflict of interest.

References

1. Bond, T.C.; Doherty, S.J.; Fahey, D.W.; Forster, P.M.; Berntsen, T.; DeAngelo, B.J.; Flanner, M.G.; Ghan, S.; Kärcher, B.; Koch, D.; et al. Bounding the role of black carbon in the climate system: A scientific assessment. *J. Geophys. Res. Atmos.* **2013**, *118*, 5380–5552. [[CrossRef](#)]
2. Ward, D.S.; Kloster, S.; Mahowald, N.M.; Rogers, B.M.; Randerson, J.T.; Hess, P.G. The changing radiative forcing of fires: Global model estimates for past, present and future. *Atmos. Chem. Phys.* **2012**, *12*, 10857–10886. [[CrossRef](#)]
3. Tosca, M.G.; Randerson, J.T.; Zender, C.S. Global impact of smoke aerosols from landscape fires on climate and the Hadley circulation. *Atmos. Chem. Phys.* **2013**, *13*, 5227–5241. [[CrossRef](#)]
4. Jiang, Y.; Lu, Z.; Liu, X.; Qian, Y.; Zhang, K.; Wang, Y.; Yang, X.-Q. Impacts of global open-fire aerosols on direct radiative, cloud and surface-albedo effects simulated with CAM5. *Atmos. Chem. Phys.* **2016**, *16*, 14805–14824. [[CrossRef](#)]
5. Sand, M.; Berntsen, T.K.; von Salzen, K.; Flanner, M.G.; Langner, J.; Victor, D.G. Response of Arctic temperature to changes in emissions of short-lived climate forcers. *Nat. Clim. Chang.* **2015**, *6*, 286–289. [[CrossRef](#)]
6. Hamilton, D.S.; Hantson, S.; Scott, C.E.; Kaplan, J.O.; Pringle, K.J.; Nieradzik, L.P.; Rap, A.; Folberth, G.A.; Spracklen, D.V.; Carslaw, K.S. Reassessment of pre-industrial fire emissions strongly affects anthropogenic aerosol forcing. *Nat. Commun.* **2018**, *9*, 3128. [[CrossRef](#)] [[PubMed](#)]
7. Thornhill, G.D.; Ryder, C.L.; Highwood, E.J.; Shaffrey, L.C.; Johnson, B.T. The effect of South American biomass burning aerosol emissions on the regional climate. *Atmos. Chem. Phys.* **2015**, *18*, 5321–5342. [[CrossRef](#)]
8. Popovicheva, O.B.; Kozlov, V.S.; Engling, G.; Diapoul, E.; Persiantseva, N.M.; Timofeev, M.A.; Fan, T.-S.; Saraga, D.; Eleftheriadis, K. Small-Scale Study of Siberian Biomass Burning: I. Smoke Microstructure. *Aerosol Air Qual. Res.* **2015**, *15*, 117–128. [[CrossRef](#)]
9. Mikhailov, E.F.; Mironova, S.; Mironov, G.; Vlasenko, S.; Panov, A.; Chi, X.; Walter, D.; Carbone, S.; Artaxo, P.; Heimann, M.; et al. Long-term measurements (2010–2014) of carbonaceous aerosol and carbon monoxide at the Zotino Tall Tower Observatory (ZOTTO) in central Siberia. *Atmos. Chem. Phys.* **2017**, *17*, 14365–14392. [[CrossRef](#)]
10. Zhuravleva, T.B.; Kabanov, D.M.; Nasrtdinov, I.M.; Russkova, T.V.; Sakerin, S.M.; Smirnov, A.; Holben, B.N. Radiative characteristics of aerosol during extreme fire event over Siberia in summer 2012. *Atmos. Meas. Tech.* **2017**, *10*, 179–198. [[CrossRef](#)]
11. Pani, S.K.; Lin, N.-H.; Chantara, S.; Wang, S.-H.; Khamkaew, C.; Prapamontol, T.; Janjai, S. Radiative response of biomass-burning aerosols over an urban atmosphere in northern peninsular Southeast Asia. *Sci. Total Environ.* **2018**, *633*, 892–911. [[CrossRef](#)]

12. Reddington, C.L.; Morgan, W.T.; Darbyshire, E.; Brito, J.; Coe, H.; Artaxo, P.; Scott, C.E.; Marsham, J.; Spracklen, D.V. Biomass burning aerosol over the Amazon: Analysis of aircraft, surface and satellite observations using a global aerosol model. *Atmos. Chem. Phys.* **2019**, *19*, 9125–9152. [[CrossRef](#)]
13. Denjean, C.; Bourrienne, T.; Burnet, F.; Mallet, M.; Maury, N.; Colomb, A.; Dominutt, P.; Brito, J.; Dupuy, R.; Sellegri, K.; et al. Overview of aerosol optical properties over southern West Africa from DACCIWA aircraft measurements. *Atmos. Chem. Phys.* **2020**, *20*, 4735–4756. [[CrossRef](#)]
14. Kleinman, L.L.; Sedlacek III, A.J.; Adachi, K.; Buseck, P.R.; Collier, S.; Dubey, M.K.; Hodshire, A.L.; Lewis, E.; Onasch, T.B.; Pierce, J.R.; et al. Rapid evolution of aerosol particles and their optical properties downwind of wildfires in the western US. *Atmos. Chem. Phys.* **2020**, *20*, 13319–13341. [[CrossRef](#)]
15. Hodshire, A.L.; Ramnarine, E.; Akherati, A.; Alvarado, M.L.; Farmer, D.K.; Jathar, S.H.; Kreidenweis, S.M.; Lonsdale, C.R.; Onasch, T.B.; Springston, S.R.; et al. Dilution impacts on smoke aging: Evidence in Biomass Burning Observation Project (BBOP) data. *Atmos. Chem. Phys.* **2021**, *21*, 6839–6855. [[CrossRef](#)]
16. Reid, J.S.; Koppmann, R.; Eck, T.F.; Eleuterio, D.P. A review of biomass burning emissions part II: Intensive physical properties of biomass burning particles. *Atmos. Chem. Phys.* **2005**, *5*, 799–825. [[CrossRef](#)]
17. Reid, J.S.; Eck, T.F.; Christopher, S.A.; Koppmann, R.; Dubovik, O.; Eleuterio, D.P.; Holben, B.N.; Reid, E.A.; Zhang, J. A review of biomass burning emissions part III: Intensive optical properties of biomass burning particles. *Atmos. Chem. Phys.* **2005**, *5*, 827–849. [[CrossRef](#)]
18. Bond, T.C.; Bergstrom, R.W. Light Absorption by Carbonaceous Particles: An Investigative Review. *Aerosol Sci. Technol.* **2006**, *40*, 27–67. [[CrossRef](#)]
19. Sayer, A.M.; Hsu, N.C.; Eck, T.F.; Smirnov, A.; Holben, B.N. AERONET-based models of smoke-dominated aerosol near source regions and transported over oceans, and implications for satellite retrievals of aerosol optical depth. *Atmos. Chem. Phys.* **2014**, *14*, 11493–11523. [[CrossRef](#)]
20. Nikonovas, T.; North, P.R.J.; Doerr, S.H. Smoke aerosol properties and ageing effects for northern temperate and boreal regions derived from AERONET source and age attribution. *Atmos. Chem. Phys.* **2015**, *15*, 7929–7943. [[CrossRef](#)]
21. Hodshire, A.; Akherati, A.; Alvarado, M.J.; Brown-Steiner, B.; Jathar, S.H.; Jimenez, J.L.; Kreidenweis, S.M.; Lonsdale, C.R.; Onasch, T.B.; Ortega, A.; et al. Aging Effects on Biomass Burning Aerosol Mass and Composition: A Critical Review of Field and Laboratory Studies. *Environ. Sci. Technol.* **2019**, *53*, 10007–10022. [[CrossRef](#)] [[PubMed](#)]
22. Cubison, M.J.; Ortega, A.M.; Hayes, P.L.; Farmer, D.K.; Day, D.; Lechner, M.J.; Brune, W.H.; Apel, E.; Diskin, G.S.; Fisher, J.A.; et al. Effects of aging on organic aerosol from open biomass burning smoke in aircraft and laboratory studies. *Atmos. Chem. Phys.* **2011**, *11*, 12049–12064. [[CrossRef](#)]
23. Hennigan, C.J.; Miracolo, M.A.; Engelhart, G.J.; May, A.A.; Presto, A.A.; Lee, T.; Sullivan, A.P.; McMeeking, G.R.; Coe, H.; Wold, C.E.; et al. Chemical and physical transformations of organic aerosol from the photo-oxidation of open biomass burning emissions in an environmental chamber. *Atmos. Chem. Phys.* **2011**, *11*, 7669–7686. [[CrossRef](#)]
24. Kononov, I.B.; Beekmann, M.; Berezin, E.V.; Petetin, H.; Mielonen, T.; Kuznetsova, I.N.; Andreae, M.O. The role of semi-volatile organic compounds in the mesoscale evolution of biomass burning aerosol: A modeling case study of the 2010 mega-fire event in Russia. *Atmos. Chem. Phys.* **2015**, *15*, 13269–13297. [[CrossRef](#)]
25. Vakkari, V.; Beukes, J.P.; Dal Maso, M.; Aurela, M.; Josipovic, M.; van Zyl, P.G. Major secondary aerosol formation in southern African open biomass burning plumes. *Nat. Geosci.* **2018**, *11*, 580–583. [[CrossRef](#)]
26. May, A.A.; Lee, T.; McMeeking, G.R.; Akagi, S.; Sullivan, A.P.; Urbanski, S.; Yokelson, R.J.; Kreidenweis, S.M. Observations and analysis of organic aerosol evolution in some prescribed fire smoke plumes. *Atmos. Chem. Phys.* **2015**, *15*, 6323–6335. [[CrossRef](#)]
27. Zhou, S.; Collier, S.; Jaffe, D.A.; Briggs, N.L.; Hee, J.; Sedlacek III, A.J.; Kleinman, L.; Onasch, T.B.; Zhang, Q. Regional influence of wildfires on aerosol chemistry in the western US and insights into atmospheric aging of biomass burning organic aerosol. *Atmos. Chem. Phys.* **2017**, *17*, 2477–2493. [[CrossRef](#)]
28. Engelhart, G.J.; Hennigan, C.J.; Miracolo, M.A.; Robinson, A.L.; Pandis, S.N. Cloud condensation nuclei activity of fresh primary and aged biomass burning aerosol. *Atmos. Chem. Phys.* **2012**, *12*, 7285–7293. [[CrossRef](#)]
29. Forrister, H.; Liu, J.; Scheuer, E.; Dibb, J.; Ziemba, L.; Thornhill, K.L.; Anderson, B.; Diskin, G.; Perring, A.E.; Schwarz, J.P.; et al. Evolution of brown carbon in wildfire plumes. *Geophys. Res. Lett.* **2015**, *42*, 4623–4630. [[CrossRef](#)]
30. Fleming, L.T.; Lin, P.; Roberts, J.M.; Selimovic, V.; Yokelson, R.; Laskin, J.; Laskin, A.; Nizkorodov, S.A. Molecular composition and photochemical lifetimes of brown carbon chromophores in biomass burning organic aerosol. *Atmos. Chem. Phys.* **2020**, *20*, 1105–1129. [[CrossRef](#)]
31. Wu, H.; Taylor, J.W.; Langridge, J.M.; Yu, C.; Allan, J.D.; Szpek, K.; Cotterell, M.I.; Williams, P.I.; Flynn, M.; Barker, P.; et al. Rapid transformation of ambient absorbing aerosols from West African biomass burning. *Atmos. Chem. Phys.* **2021**, *21*, 9417–9440. [[CrossRef](#)]
32. Akagi, S.K.; Craven, J.S.; Taylor, J.W.; McMeeking, G.R.; Yokelson, R.J.; Burling, I.R.; Urbanski, S.P.; Wold, C.E.; Seinfeld, J.H.; Coe, H.; et al. Evolution of trace gases and particles emitted by a chaparral fire in California. *Atmos. Chem. Phys.* **2012**, *12*, 1397–1421. [[CrossRef](#)]
33. Kononov, I.B.; Beekmann, M.; Berezin, E.V.; Formenti, P.; Andreae, M.O. Probing into the aging dynamics of biomass burning aerosol by using satellite measurements of aerosol optical depth and carbon monoxide. *Atmos. Chem. Phys.* **2017**, *17*, 4513–4537. [[CrossRef](#)]

34. Kononov, I.B.; Golovushkin, N.A.; Beekmann, M.; Andreae, M.O. Insights into the aging of biomass burning aerosol from satellite observations and 3D atmospheric modeling: Evolution of the aerosol optical properties in Siberian wildfire plumes. *Atmos. Chem. Phys.* **2021**, *21*, 357–392. [[CrossRef](#)]
35. Tsigaridis, K.; Daskalakis, N.; Kanakidou, M.; Adams, P.J.; Artaxo, P.; Bahadur, R.; Balkanski, Y.; Bauer, S.E.; Bellouin, N.; Benedetti, A.; et al. The AeroCom evaluation and intercomparison of organic aerosol in global models. *Atmos. Chem. Phys.* **2014**, *14*, 10845–10895. [[CrossRef](#)]
36. Tsigaridis, K.; Kanakidou, M. The Present and Future of Secondary Organic Aerosol Direct Forcing on Climate. *Curr. Clim. Chang. Rep.* **2018**, *4*, 84–98. [[CrossRef](#)]
37. Hodzic, A.; Campuzano-Jost, P.; Bian, H.; Chin, M.; Colarco, P.R.; Day, D.A.; Froyd, K.D.; Heinold, B.; Jo, D.S.; Katich, J.M.; et al. Characterization of organic aerosol across the global remote troposphere: A comparison of ATom measurements and global chemistry models. *Atmos. Chem. Phys.* **2020**, *20*, 4607–4635. [[CrossRef](#)]
38. Robinson, A.L.; Donahue, N.M.; Shrivastava, M.K.; Weitkamp, E.A.; Sage, A.M.; Grieshop, A.P.; Lane, T.E.; Pierce, J.R.; Pandis, S.N. Rethinking organic aerosols: Semivolatile emissions and photochemical aging. *Science* **2007**, *315*, 1259–1262. [[CrossRef](#)] [[PubMed](#)]
39. Shrivastava, M.; Easter, R.; Liu, X.; Zelenyuk, A.; Singh, B.; Zhang, K.; Ma, P.-L.; Chand, D.; Ghan, S.; Jimenez, J.L.; et al. Global transformation and fate of SOA: Implications of low volatility SOA and gas phase fragmentation reactions. *J. Geophys. Res. Atmos.* **2015**, *120*, 4169–4195. [[CrossRef](#)]
40. May, A.A.; Levin, E.J.T.; Hennigan, C.J.; Riipinen, I.; Lee, T.; Collett, J.L., Jr.; Jimenez, J.L.; Kreidenweis, S.M.; Robinson, A.L. Gas-particle partitioning of primary organic aerosol emissions: 3. Biomass burning. *J. Geophys. Res. Atmos.* **2013**, *118*, 11327–11338. [[CrossRef](#)]
41. Lee-Taylor, J.; Madronich, S.; Aumont, B.; Baker, A.; Camredon, M.; Hodzic, A.; Tyndall, G.S.; Apel, E.; Zaveri, R.A. Explicit modeling of organic chemistry and secondary organic aerosol partitioning for Mexico City and its outflow plume. *Atmos. Chem. Phys.* **2011**, *11*, 13219–13241. [[CrossRef](#)]
42. Lee-Taylor, J.; Hodzic, A.; Madronich, S.; Aumont, B.; Camredon, M.; Valorso, R. Multiday production of condensing organic aerosol mass in urban and forest outflow. *Atmos. Chem. Phys.* **2015**, *15*, 595–615. [[CrossRef](#)]
43. Ciarelli, G.; El Haddad, I.; Bruns, E.; Aksoyoglu, S.; Möhler, O.; Baltensperger, U.; Prévôt, A.S.H. Constraining a hybrid volatility basis-set model for aging of wood-burning emissions using smog chamber experiments: A box-model study based on the VBS scheme of the CAMx model (v5.40). *Geosci. Model Dev.* **2017**, *10*, 2303–2320. [[CrossRef](#)]
44. Bian, Q.; Jathar, S.H.; Kodros, J.K.; Barsanti, K.C.; Hatch, L.E.; May, A.A.; Kreidenweis, S.M.; Pierce, J.R. Secondary organic aerosol formation in biomass-burning plumes: Theoretical analysis of lab studies and ambient plumes. *Atmos. Chem. Phys.* **2017**, *17*, 5459–5475. [[CrossRef](#)]
45. Hodshire, A.L.; Bian, Q.; Ramnarine, E.; Lonsdale, C.R.; Alvarado, M.J.; Kreidenweis, S.M.; Jathar, S.H.; Pierce, J.R. More than emissions and chemistry: Fire size, dilution, and background aerosol also greatly influence near-field biomass burning aerosol aging. *J. Geophys. Res. Atmos.* **2019**, *124*, 5589–5611. [[CrossRef](#)]
46. Kononov, I.B.; Beekmann, M.; Golovushkin, N.A.; Andreae, M.O. Nonlinear behavior of organic aerosol in biomass burning plumes: A microphysical model analysis. *Atmos. Chem. Phys.* **2019**, *19*, 12091–12119. [[CrossRef](#)]
47. Stefenelli, G.; Jiang, J.; Bertrand, A.; Bruns, E.A.; Pieber, S.M.; Baltensperger, U.; Marchand, N.; Aksoyoglu, S.; Prévôt, A.S.H.; Slowik, J.G.; et al. Secondary organic aerosol formation from smoldering and flaming combustion of biomass: A box model parametrization based on volatility basis set. *Atmos. Chem. Phys.* **2019**, *19*, 11461–11484. [[CrossRef](#)]
48. García, O.E.; Díaz, J.P.; Expósito, F.J.; Díaz, A.M.; Dubovik, O.; Derimian, Y.; Dubuisson, P.; Roger, J.-C. Shortwave radiative forcing and efficiency of key aerosol types using AERONET data. *Atmos. Chem. Phys.* **2012**, *12*, 5129–5145. [[CrossRef](#)]
49. Kononov, I.B.; Golovushkin, N.A.; Beekmann, M.; Panchenko, M.V.; Andreae, M.O. Inferring the absorption properties of organic aerosol in biomass burning plumes from remote optical observations. *Atmos. Meas. Tech.* **2021**, *14*, 6647–6673. [[CrossRef](#)]
50. Hand, J.L.; Day, D.E.; McMeeking, G.M.; Levin, E.J.T.; Carrico, C.M.; Kreidenweis, S.M.; Malm, W.C.; Laskin, A.; Desyaterik, Y. Measured and modeled humidification factors of fresh smoke particles from biomass burning: Role of inorganic constituents. *Atmos. Chem. Phys.* **2010**, *10*, 6179–6194. [[CrossRef](#)]
51. Stromatas, S.; Turquety, S.; Menut, L.; Chepfer, H.; Péré, J.C.; Cesana, G.; Bessagnet, B. Lidar signal simulation for the evaluation of aerosols in chemistry transport models. *Geosci. Model Dev.* **2012**, *5*, 1543–1564. [[CrossRef](#)]
52. Tsimpidi, A.P.; Karydis, V.A.; Pozzer, A.; Pandis, S.N.; Lelieveld, J. ORACLE 2-D (v2.0): An efficient module to compute the volatility and oxygen content of organic aerosol with a global chemistry–climate model. *Geosci. Model Dev.* **2018**, *11*, 3369–3389. [[CrossRef](#)]
53. Majdi, M.; Turquety, S.; Sartelet, K.; Legorgeu, C.; Menut, L.; Kim, Y. Impact of wildfires on particulate matter in the Euro-Mediterranean in 2007: Sensitivity to some parameterizations of emissions in air quality models. *Atmos. Chem. Phys.* **2019**, *19*, 785–812. [[CrossRef](#)]
54. Jiang, J.; El Haddad, I.; Aksoyoglu, S.; Stefenelli, G.; Bertrand, A.; Marchand, N.; Canonaco, F.; Petit, J.-E.; Favez, O.; Gilardoni, S.; et al. Influence of biomass burning vapor wall loss correction on modeling organic aerosols in Europe by CAMx v6.50. *Geosci. Model Dev.* **2021**, *14*, 1681–1697. [[CrossRef](#)]
55. Ahern, A.T.; Robinson, E.S.; Tkacik, D.S.; Saleh, R.; Hatch, L.E.; Barsanti, K.C.; Stockwell, C.E.; Yokelson, R.J.; Presto, A.A.; Robinson, A.L.; et al. Production of secondary organic aerosol during aging of biomass burning smoke from fresh fuels and its relationship to VOC precursors. *J. Geophys. Res.* **2019**, *124*, 3583–3606. [[CrossRef](#)]

56. Kodros, J.K.; Papanastasiou, D.K.; Paglione, M.; Masiol, M.; Squizzato, S.; Florou, K.; Skyllakou, K.; Kaltsonoudis, C.; Nenes, A.; Pandis, S.N. Rapid dark aging of biomass burning as an overlooked source of oxidized organic aerosol. *Proc. Natl. Acad. Sci. USA* **2020**, *117*, 33028–33033. [CrossRef]
57. Golovushkin, N.A.; Konovalov, I.B. Nonlinear features of the atmospheric evolution of the absorption properties of biomass burning aerosol. In Proceedings of the 26th International Symposium on Atmospheric and Ocean Optics, Atmospheric Physics, Moscow, Russia, 6–10 July 2020; p. 11560C. [CrossRef]
58. Golovushkin, N.A.; Kuznetsova, I.N.; Konovalov, I.B.; Kozlov, V.S.; Nakhaev, M.I. Analysis of brown carbon content and evolution in smokes from Siberian forest fires using AERONET measurements. *Atmos. Ocean. Opt.* **2020**, *33*, 267–273. [CrossRef]
59. Köpke, P.; Hess, M.; Schult, I.; Shettle, E.P. Global Aerosol Data Set. Report No. 2431997. pp. 1–44. Available online: https://mpimet.mpg.de/fileadmin/publikationen/Reports/MPI-Report_243.pdf (accessed on 16 October 2021).
60. Zhuravleva, T.B.; Kabanov, D.M.; Sakerin, S.M.; Firsov, K.M. Simulation of Aerosol Direct Radiative Forcing under Typical Summer Conditions of Siberia. Part 1. Method of Calculation and Choice of Input Parameters. *Atmos. Ocean. Opt.* **2009**, *22*, 63–73. [CrossRef]
61. Panchenko, M.V.; Zhuravleva, T.B.; Terpugova, S.A.; Polkin, V.V.; Kozlov, V.S. An empirical model of optical and radiative characteristics of the tropospheric aerosol over West Siberia in summer. *Atmos. Meas. Tech.* **2012**, *5*, 1513–1527. [CrossRef]
62. Slingo, A. A GCM parameterization for shortwave radiative properties of water clouds. *J. Atmos. Sci.* **1989**, *46*, 1419–1427. [CrossRef]
63. Lacis, A.A.; Oinas, V. A description of the k-distribution method for modelling nongray gaseous absorption, thermal emission, and multiple scattering in vertically inhomogeneous atmospheres. *J. Geophys. Res.* **1991**, *96*, 9027–9063. [CrossRef]
64. Ricchiuzzi, P.; Yang, S.; Gautier, C.; Sowle, D. SBDART: A research and teaching software tool for plane-parallel radiative transfer in the Earth's atmosphere. *Bull. Am. Meteorol. Soc.* **1998**, *79*, 2101–2114. [CrossRef]
65. Clough, S.A.; Shephard, M.W.; Mlawer, E.J.; Delamere, J.S.; Iacono, M.J.; Cady-Pereira, K.; Boukabara, S.; Brown, P.D. Atmospheric radiative transfer modeling: A summary of the AER codes. *J. Quant. Spectrosc. Radiat. Transf.* **2004**, *91*, 233–244. [CrossRef]
66. Mayer, B.; Kylling, A. Technical note: The libRadtran software package for radiative transfer calculations—Description and examples of use. *Atmos. Chem. Phys.* **2005**, *5*, 1855–1877. [CrossRef]
67. Tvorogov, S.D.; Zhuravleva, T.B.; Rodimova, O.B.; Firsov, K.M. Theory of series of exponents and its application for analysis of radiation processes. In *Global Climatology and Ecodynamics: Anthropogenic Effects on the State of Planet Earth*; Cracknell, A.P., Krapivin, V.F., Varotsos, C.A., Eds.; Springer: Chichester, UK; Praxis: Chichester, UK, 2009; pp. 211–240. [CrossRef]
68. Zhuravleva, T.B.; Sakerin, S.M.; Bedareva, T.V.; Kabanov, D.M.; Nasrtdinov, I.M.; Chesnokova, T.Y. Solar Radiative Fluxes in the Clear-Sky Atmosphere of Western Siberia: A Comparison of Simulations with Field Measurements. *Atmos. Ocean. Opt.* **2014**, *27*, 176–186. [CrossRef]
69. Zhuravleva, T.B.; Nasrtdinov, I.M.; Vinogradova, A.A. Direct Radiative Effects of Smoke Aerosol in the Region of Tiksi Station (Russian Arctic): Preliminary Results. *Atmos. Ocean. Opt.* **2019**, *32*, 296–305. [CrossRef]
70. Hess, M.; Koepke, P.; Schult, I. Optical properties of aerosols and clouds: The software package OPAC. *Bull. Am. Meteorol. Soc.* **1998**, *79*, 831–844. [CrossRef]
71. Rothman, L.S.; Gordon, I.E.; Babikov, Y.; Barbe, A.; Chris Benner, D.; Bernath, P.F.; Birk, M.; Bizzocchi, L.; Boudon, V.; Brown, L.R.; et al. The HITRAN2012 molecular spectroscopic database. *J. Quant. Spectrosc. Radiat. Transf.* **2013**, *130*, 4–50. [CrossRef]
72. Mlawer, E.J.; Payne, V.H.; Moncet, J.-L.; Delamere, J.S.; Alvarado, M.J.; Tobin, D.C. Development and recent evaluation of the MT_CKD model of continuum absorption. *Philos. Trans. R. Soc. A* **2012**, *370*, 2520–2556. [CrossRef]
73. Komarov, V.S.; Lomakina, N.Y. *Statistical Models of the Atmospheric Boundary Layer*; IAO Publishing House: Tomsk, Russia, 2008; p. 222. (In Russian)
74. Anderson, G.; Clough, S.; Kneizys, F.; Chetwynd, J.; Shettle, E. *AFGL Atmospheric Constituent Profiles (0–120 km)*; Air force Geophysics Laboratory: Hanscom AFB, MA, USA, 1986; pp. 1–43.
75. Kabanov, D.M.; Sakerin, S.M.; Turchinovich, Y.S. Interannual and Seasonal Variations in the Atmospheric Aerosol Optical Depth in the Region of Tomsk (1995–2018). *Atmos. Ocean. Opt.* **2019**, *32*, 663–670. [CrossRef]
76. Antokhina, O.Y.; Antokhin, P.N.; Arshinova, V.G.; Arshinov, M.Y.; Belan, B.D.; Belan, S.B.; Davydov, D.K.; Dudorova, N.V.; Ivlev, G.A.; Kozlov, A.V.; et al. Dynamics of the greenhouse gas concentrations in Western Siberia. *Opt. Atmos. Okeana* **2019**, *32*, 777–785. (In Russian) [CrossRef]
77. Bazhenov, O.E.; Burlakov, V.D.; Grishaev, M.V.; Gridnev, Y.V.; Dolgii, S.I.; Makeev, A.P.; Nevzorov, A.V.; Salnikova, N.S.; Trifonov, D.A.; Arshinov, M.Y.; et al. Comparison of remote spectrophotometric and lidar measurements of O₃, NO₂, temperature, and stratospheric aerosol with data of satellite and radiosonde measurements. *Opt. Atmos. Okeana* **2016**, *29*, 216–223. (In Russian) [CrossRef]
78. Fontenla, J.; White, O.R.; Fox, P.A.; Avert, E.H.; Kurucz, R.L. Calculation of solar irradiances, I. Synthesis of the solar spectrum. *Astrophys. J.* **1999**, *518*, 480–500. [CrossRef]
79. Baldridge, A.M.; Hook, S.J.; Grove, C.I.; Rivera, G. The ASTER spectral library version 2.0. *Remote Sens. Environ.* **2009**, *113*, 711–715. [CrossRef]
80. Markowicz, K.M.; Flatau, P.J.; Quinn, P.K.; Carrico, C.M.; Flatau, M.K.; Vogelmann, A.M.; Bates, D.; Liu, M.; Rood, M.J. Influence of relative humidity on aerosol radiative forcing: An ACE-Asia experiment perspective. *J. Geophys. Res.* **2003**, *108*, 8662. [CrossRef]

81. Conant, W.C.; Seinfeld, J.H.; Wang, J.; Carmichael, G.R.; Tang, Y.; Uno, I.; Flatau, P.J.; Markowicz, K.M.; Quinn, P.K. A model for the radiative forcing during ACE-Asia derived from CIRPAS Twin Otter and R/V Ronald H. Brown data and comparison with observations. *J. Geophys. Res.* **2003**, *108*, 8661. [[CrossRef](#)]
82. Lisok, J.; Rozwadowska, A.; Pedersen, J.G.; Markowicz, K.M.; Ritter, C.; Kaminski, J.W.; Struzewska, J.; Mazzola, M.; Udisti, R.; Becagli, S.; et al. Radiative impact of an extreme Arctic biomass-burning event. *Atmos. Chem. Phys.* **2018**, *18*, 8829–8848. [[CrossRef](#)]
83. Stone, R.; Anderson, G.; Shettle, E.; Andrews, E.; Loukachine, K.; Dutton, E.; Schaaf, C.; Roman, M. Radiative impact of boreal smoke in the Arctic: Observed and modeled. *J. Geophys. Res.* **2008**, *113*, D14S16. [[CrossRef](#)]
84. Chubarova, N.; Nezval, Y.; Sviridenkov, M.; Smirnov, A.; Slutsker, I. Smoke aerosol and its radiative effects during extreme fire event over Central Russia in summer 2010. *Atmos. Meas. Tech.* **2012**, *5*, 557–568. [[CrossRef](#)]
85. McComiskey, A.; Schwartz, S.E.; Schmid, B.; Guan, H.; Lewis, E.R.; Ricchiazzi, P.; Ogren, J.A. Direct aerosol forcing: Calculation from observables and sensitivities to inputs. *J. Geophys. Res.* **2008**, *113*, D09202. [[CrossRef](#)]
86. Di Biagio, C.; di Sarra, A.; Meloni, D. Large atmospheric shortwave radiative forcing by Mediterranean aerosols derived from simultaneous ground-based and spaceborne observations and dependence on the aerosol type and single scattering albedo. *J. Geophys. Res.* **2010**, *115*, D10209. [[CrossRef](#)]
87. Di Biagio, C.; Formenti, P.; Doppler, L.; Gaimoz, C.; Grand, N.; Ancellet, G.; Attié, J.-L.; Bucci, S.; Dubuisson, P.; Fierli, F.; et al. Continental pollution in the Western Mediterranean basin: Large variability of the aerosol single scattering albedo and influence on the direct shortwave radiative effect. *Atmos. Chem. Phys.* **2016**, *16*, 10591–10607. [[CrossRef](#)]
88. Kuang, Y.; Zhao, C.S.; Tao, J.C.; Ma, N. Diurnal variations of aerosol optical properties in the North China Plain and their influences on the estimates of direct aerosol radiative effect. *Atmos. Chem. Phys.* **2015**, *15*, 5761–5772. [[CrossRef](#)]
89. Tomasi, C.; Lanconelli, C.; Mazzola, M. Dependence of direct aerosol radiative forcing on the optical properties of atmospheric aerosol and underlying surface. In *Radiative Transfer and Light Scattering*; Springer Praxis Books/Environmental Sciences; Kokhanovsky, A.A., Ed.; Springer: Berlin/Heidelberg, Germany, 2013; Volume 8, Chapter 11; pp. 505–626. [[CrossRef](#)]
90. Schulz, M.; Textor, C.; Kinne, S.; Balkanski, Y.; Bauer, S.; Bernsten, T.; Berglen, T.; Boucher, O.; Dentener, F.; Guibert, S.; et al. Radiative forcing by aerosols as derived from the AeroCom present-day and pre-industrial simulations. *Atmos. Chem. Phys.* **2006**, *6*, 5225–5246. [[CrossRef](#)]
91. Verma, S.; Prakash, D.; Srivastava, A.K.; Payra, S. Radiative Forcing Estimation of Aerosols at an Urban Site near the Thar Desert Using Ground-Based Remote Sensing Measurements. *Aerosol Air Qual. Res.* **2017**, *17*, 1294–1304. [[CrossRef](#)]
92. Xie, Y.; Li, Z.; Li, L.; Wagener, R.; Abboud, I.; Li, K.; Li, D.; Zhang, Y.; Chen, X.; Xu, H. Aerosol optical, microphysical, chemical and radiative properties of high aerosol load cases over the Arctic based on AERONET measurements. *Sci. Rep.* **2018**, *8*, 9376. [[CrossRef](#)] [[PubMed](#)]
93. Tian, P.; Zhang, L.; Ma, J.; Tang, K.; Xu, L.; Wang, Y.; Cao, X.; Liang, J.; Ji, Y.; Jiang, J.H.; et al. Radiative absorption enhancement of dust mixed with anthropogenic pollution over East Asia. *Atmos. Chem. Phys.* **2018**, *18*, 7815–7825. [[CrossRef](#)]
94. Sartelet, K.; Couvidat, F.; Wang, Z.; Flageul, C.; Kim, Y. SSH-Aerosol v1.1: A Modular Box Model to Simulate the Evolution of Primary and Secondary Aerosols. *Atmosphere* **2020**, *11*, 525. [[CrossRef](#)]
95. Shi, S.; Cheng, T.; Gu, X.; Guo, H.; Wu, Y.; Wang, Y. Biomass burning aerosol characteristics for different vegetation types in different aging periods. *Environ. Int.* **2019**, *126*, 504–511. [[CrossRef](#)]
96. Sakamoto, K.M.; Laing, J.R.; Stevens, R.G.; Jaffe, D.A.; Pierce, J.R. The evolution of biomass-burning aerosol size distributions due to coagulation: Dependence on fire and meteorological details and parameterization. *Atmos. Chem. Phys.* **2016**, *16*, 7709–7724. [[CrossRef](#)]
97. Lin, J.J.; Kenneth, E.N.; Holsen, T.M. Dry deposition velocities as a function of particle size in the ambient atmosphere. *Aerosol. Sci. Technol.* **2007**, *20*, 239–252. [[CrossRef](#)]
98. Shiraiwa, M.; Li, Y.; Tsimpidi, A.P.; Karydis, V.A.; Berkemeier, T.; Pandis, S.N.; Lelieveld, J.; Koop, T.; Pöschl, U. Global distribution of particle phase state in atmospheric secondary organic aerosols. *Nat. Commun.* **2017**, *8*, 15002. [[CrossRef](#)] [[PubMed](#)]
99. Kim, Y.; Sartelet, K.; Couvidat, F. Modeling the effect of nonideality, dynamic mass transfer and viscosity on SOA formation in a 3-D air quality model. *Atmos. Chem. Phys.* **2019**, *19*, 1241–1261. [[CrossRef](#)]
100. Song, C.; Zaveri, R.A.; Alexander, M.L.; Thornton, J.A.; Madronich, S.; Ortega, J.V.; Zelenyuk, A.; Yu, X.-Y.; Laskin, A.; Maughan, D.A. Effect of hydrophobic primary organic aerosols on secondary organic aerosol formation from ozonolysis of α -pinene. *Geophys. Res. Lett.* **2007**, *34*, L20803. [[CrossRef](#)]
101. Hodzic, A.; Madronich, S.; Kasibhatla, P.S.; Tyndall, G.; Aumont, B.; Jimenez, J.L.; Lee-Taylor, J.; Orlando, J. Organic photolysis reactions in tropospheric aerosols: Effect on secondary organic aerosol formation and lifetime. *Atmos. Chem. Phys.* **2015**, *15*, 9253–9269. [[CrossRef](#)]
102. Feng, Y.; Ramanathan, V.; Kotamarthi, V.R. Brown carbon: A significant atmospheric absorber of solar radiation? *Atmos. Chem. Phys.* **2013**, *13*, 8607–8621. [[CrossRef](#)]
103. Wang, X.; Heald, C.L.; Liu, J.; Weber, R.J.; Campuzano-Jost, P.; Jimenez, J.L.; Schwarz, J.P.; Perring, A.E. Exploring the observational constraints on the simulation of brown carbon. *Atmos. Chem. Phys.* **2018**, *18*, 635–653. [[CrossRef](#)]